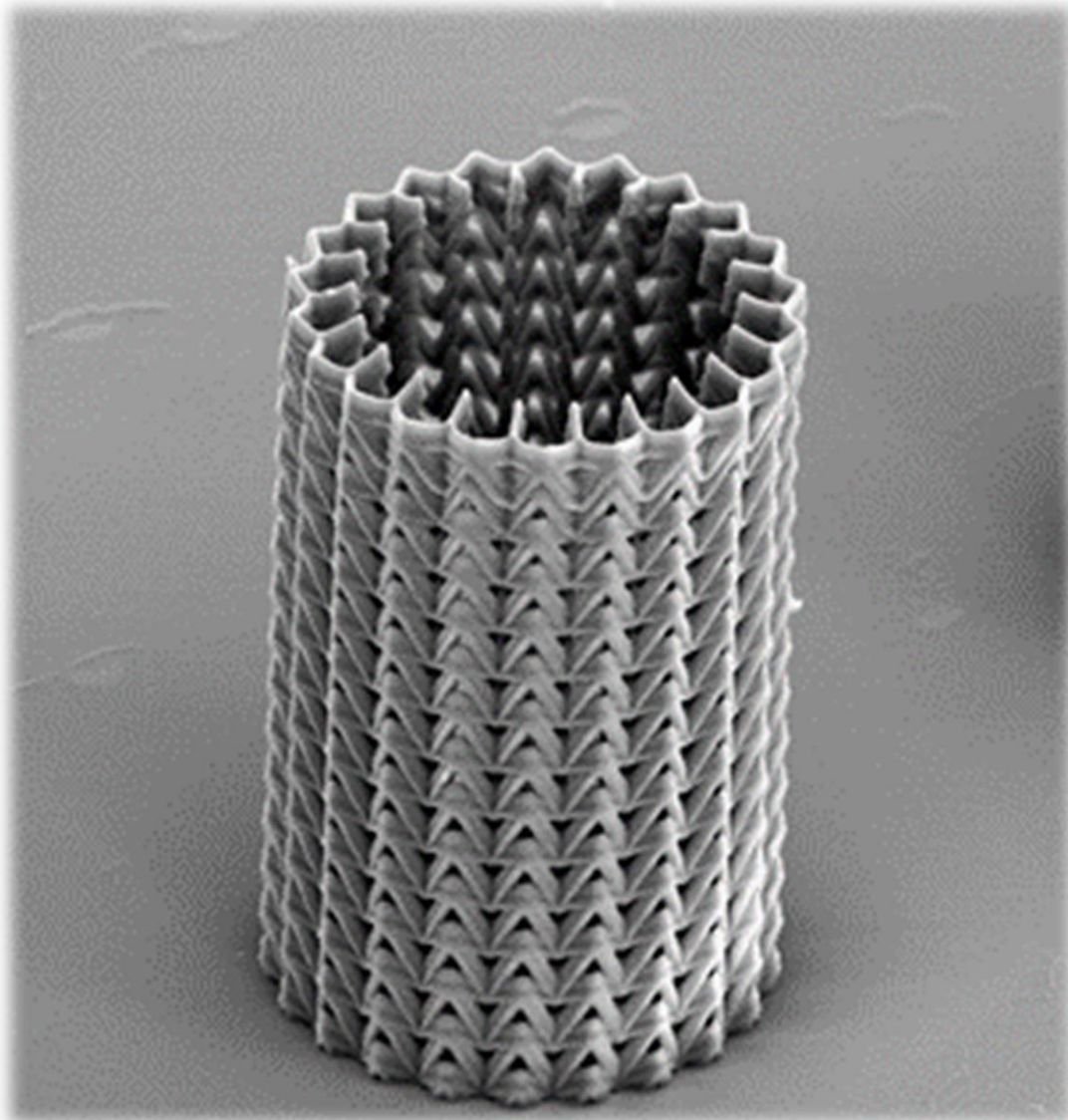


3D MECHANICAL METAMATERIALS



Student: Ioannis Spanos, 618

University of Crete,
Department of Physics
"Photonics and Nanoelectronics"

Supervisors: Dr. Maria Farsari
Dr. Vasileia Melissinaki

Committee: Prof. Dimitris Charalambidis
Dr. Emmanuel Stratakis
Dr. Maria Farsari

CONTENTS

ABSTRACT

INTRODUCTION

- **CHAPTER 1:** VISCOELASTIC MATERIALS
- **CHAPTER 2:** MULTIPHOTON LITHOGRAPHY
- **CHAPTER 3:** HYBRID MATERIALS
- **CHAPTER 4:** EXPERIMENTAL SETUP
- **CHAPTER 5:** COMPUTATIONAL TOOLS
- **CHAPTER 6:** RESULTS and DISCUSSION

CONCLUSIONS and FUTURE PROSPECTS

REFERENCES

ΕΥΧΑΡΙΣΤΙΕΣ

Η εκπόνηση της παρούσας μεταπτυχιακής εργασίας δεν θα ήταν εφικτή χωρίς την συμπαράσταση και την καθοδήγηση κάποιων ατόμων. Θα ήθελα λοιπόν, ως ελάχιστη ένδειξη ευγνωμοσύνης, να τους δώσω ένα θερμό «ευχαριστώ» για την βοήθεια και τις γνώσεις που μου παρείχαν. Την Δρ. Μαρία Φαρσάρη, ερευνητικός διευθυντής και αρχηγός της ομάδας «Μη-γραμμικής Λιθογραφίας» στο Ινστιτούτο Ηλεκτρονικής Δομής και Laser, FORTH, για την ευκαιρία που μου έδωσε να δουλέψω στο εργαστήριο της για άλλη μία φορά, την Δρ. Βασιλεία Μελισσινάκη για την έμπρακτη και αποδοτική καθοδήγηση της σε όποιο ερευνητικό θέμα εμφανιζόταν, καθώς και τα υπόλοιπα μέλη της ομάδας, που με την προθυμία και την αυταπάρνηση τους συνείσφεραν στην ομαλή διεξαγωγή της εργασίας, καθ' όλη την παραμονή μου στο εργαστήριο, παρ' όλα τα όποια προβλήματα προέκυψαν στην πορεία. Την κα. Αλέκα Μανουσάκη, για την επαγγελματική συνεργασία και την ανατροφοδότηση που παρείχε όσο αναφορά το ηλεκτρονικό μικροσκόπιο σάρωσης. Τέλος, τους καθ. Κώστα Γρηγορόπουλο και κ. Ζαχαρία Βαγγελάτο, UC, Berkeley, για την άψογη και εποικοδομητική τους συνεργασία στις μετρήσεις *nano-DMA*, που αποτέλεσαν αναπόσπαστο συστατικό της παρούσας εργασίας.

ΠΕΡΙΛΗΨΗ

Στην παρούσα εργασία, η *Πολυφωτονική Λιθογραφία* χρησιμοποιήθηκε για να κατασκευάσει 3D μηχανικά μετά-υλικά σε κλίμακα μμ. Η *Πολυφωτονική Λιθογραφία* είναι μία καθιερωμένη μέθοδος κατασκευής, ικανή να δημιουργήσει μικρο-δομές με ανάλυση που υπερβαίνει τα μερικά δεκάδες nm. Η μηχανική απόκριση των μετά-υλικών μετρήθηκε στη συνέχεια με *nano-Δυναμική Μηχανική Ανάλυση*. Η *nano-Δυναμική Μηχανική Ανάλυση* είναι μία αναδυόμενη τεχνολογία η οποία μπορεί να εκτελεί ακριβή χαρακτηρισμό των μηχανικών ιδιοτήτων ενός υλικού στη νάνο-κλίμακα. Επιπροσθέτως, η παραμόρφωση των μικρο-δομών παρατηρείται και καταγράφεται σε πραγματικό χρόνο από ένα ηλεκτρονικό μικροσκόπιο σάρωσης Quanta 3D FEG. Για πρώτη φορά από όσο γνωρίζουμε, οι μηχανικές ιδιότητες του φωτοπολυμερίσιμου υλικού που χρησιμοποιείται στην *Πολυφωτονική Λιθογραφία* χαρακτηρίστηκαν. Οι παράγοντες απώλειας και αποθήκευσης, η σκληρότητα και ο λόγος Poisson συναρτήσκει της ισχύς του λέιζερ προσδιορίστηκαν διεξοδικά και με ακρίβεια. Οι μικρο-δομές υπό διερεύνηση, που περιλαμβάνουν το φημισμένο 'παπιγιόν', σκελετικές οκτάεδρες δομές, την επανεισερχόμενη τριγωνική γεωμετρία, μια πρωτοποριακή περιστρεφόμενη δομή και ένα όργανο διάνοιξης αρτηριών με αυξητικές ιδιότητες, έχουν μέγεθος μόνο μερικά μμ. Τα μηχανικά μετά-υλικά έχουν πολυάριθμες ενδεχόμενες εφαρμογές στην ιατρική, στην βιολογία, στα ηλεκτρονικά, στις υποδομές και στην αεροναυπηγική. Έχουν ανώτερη αντοχή και απορρόφηση δονήσεων, ιδιότητες που μπορούν να χρησιμοποιηθούν σε σωματική και σεισμική προστασία. Η πορώδης και ξεχωριστή αρχιτεκτονική τους θυμίζει αυτή των οστών ή άλλων μελών του σώματος, πράγμα που τα καταστεί εξαιρετικούς υποψήφιους για εφαρμογές στη μηχανική οστών και ιστών. Η αντίθετη προς τα ένστικτα κίνηση του αρνητικού δείκτη Poisson μπορεί να χρησιμοποιηθεί σε όργανα διάνοιξης αρτηριών, ρυθμιζόμενα φίλτρα και ακριβή κινηματικά εξαρτήματα.

ABSTRACT

In the presented work, *Multiphoton Lithography (MPL)* was used to fabricate 3D *mechanical metamaterials* in the μm scale. *MPL* is a well-established fabrication method, capable of creating microstructures with a resolution exceeding a few decades nm. The mechanical response of the *metamaterials* was later measured with *nano-Dynamic Mechanical Analysis (nano-DMA)*. *Nano-DMA* is an emerging technology that can perform accurate nanoscale characterization of a material's mechanical properties. Additionally, the deformation of the microstructures is observed and recorded real-time with a Quanta 3D FEG. For the first time to our knowledge, the mechanical properties of the photopolymerizable resin used in *MPL* are properly characterized. Loss and Storage modulus, Hardness and Poisson's ratio were thoroughly and accurately determined as a function of laser power. The investigated microstructures, which include the infamous 'bowtie', truss-like octahedra structures, the re-entrant triangular geometry, a pioneered rotating structure and a stent with *auxetic* properties, are a few μm in size. *Mechanical metamaterials* have numerous potential applications in medicine, biology, electronics, infrastructure and aerospace. They possess superior durability and vibration absorption which can be employed in body and seismic protection. Their porous and unique architecture often resembles that of bones or other body parts, which makes them prime candidates for bone or tissue engineering. The counter-intuitive motion of negative Poisson's ratio can be used in stents, tunable filters and precise actuators.

INTRODUCTION

Metamaterials are artificial materials, specifically engineered to have a property not found in nature. These, often counter-intuitive, properties are achieved with unique architecture, rather than chemical composition. In the same manner common materials consist of periodic arrays of atoms, *metamaterials* are made of meta-atoms. The shape, geometry, size and orientation of these meta-atoms are what define the properties of the *metamaterial*. Initially, *metamaterials* were investigated in the field of electromagnetism during the 20th century, in which both theoretical and experimental research aimed at the manipulation of electromagnetic waves. This was an issue of how much and how accurately a material's permittivity, ϵ , and permeability, μ , could be controlled. At the time, it was known that negative permittivity could be obtained from some natural materials or periodic arrays of metallic wires, but negative permeability proved to be the real challenge. This breakthrough was achieved by J. Pendry et al in 1999 with the introduction of C-shaped rings called split ring resonators [1]. The tunability of ϵ and μ paved the path for photonic crystals, cloaking devices, super-lens and dielectric mirrors, to name a few. Over the years the concept of artificially engineered materials has spread in other areas. One of these developing fields is that of *mechanical metamaterials*. In analogy with the negative values of ϵ and μ , *mechanical metamaterials* refer to structures that exhibit unusual mechanical properties, such as vanishing shear modulus (pentamode) [2–4], negative compressibility [5–7], negative thermal expansion [8], negative Poisson's ratio (*auxetic*) [9–13] and strong-lightweight materials [14–16]. *Mechanical metamaterials* use relatively ordered hollow lattices which allow a high degree of customizability over their architecture.

The term strong-lightweight refers to exceptional mechanical properties of materials that simultaneously have low weight. From an engineering perspective, this can be expressed by the stiffness (or Young's modulus) to density ratio, E/ρ . It is natural to expect the mechanical strength of materials to degrade as their density is reduced. However, it has been proved that with the appropriate architecture, high stiffness and strength, even at low densities, can be achieved [17]. Strong-lightweight materials are divided in different categories, with respect to their design principle. The most straight-forward of them is that of micro/nanolattices, in which a unit cell with micro/nanofeatures is repeated to create a lattice in 3D space. As it stands, the geometry of the unit cell and the way it fills space are the most significant aspects in the resulting properties of the material. The octet-truss lattice is a prime example of this category [14]. The hollow nature of the lattice allows it to elastically deform due to buckling, instead of brittle fracturing. It has been shown that the lattice can fully recover even after withstanding strains of 50% [17]. The rods that constitute the structure can be made hollow. Their wall thickness affects the mechanical response of the entire structure [16]. Due to the plethora of design choices, research of micro/nanolattices can go any direction. Strong-lightweight properties can also be achieved with chiral materials [18–20]. These two-dimensional structures are comprised of nodes and ligaments which can rotate around them. Depending on their configuration they are divided in chiral and anti-chiral systems. The structure responds to stress by rotating the nodes and flexing the ligaments. Chiral materials can combine a high E/ρ ratio with the property of negative Poisson's ratio, which will be discussed later. An unexpected entry for strong-lightweight materials is that of origami structures. The art of paper-folding can be utilized in *mechanical metamaterials* for beyond-aesthetic reasons. The most prominent patterns are the periodic Miura-ori, the non-periodic Ron Resch and the square twist with a single loop design [21,22]. Their folding mechanism can give rise to increased stiffness, all the while enabling a high degree of customization. A related topic to strong-lightweight materials is the tunability of stiffness and, by extension, other mechanical properties. This exquisite property has been observed in pattern transformation structures. In particular, holey sheets or other periodic patterns of this sort change their effective stiffness as they switch

to different phases [23]. The tunability greatly depends on the shape and the arrangement of the holes. Remote variation of the stiffness was demonstrated by using a magnet [24]. Strong-lightweight *metamaterials* could improve the performance of structural components [25] and energy absorbers [26] or be used for the fabrication of biomaterials for tissue engineering applications [27].

Fluids exhibit small to no resistance to shear forces, but it is hard to compress them. In other words, their shear modulus is close to zero, while their bulk modulus is large. Solids can reproduce this behaviour by exhibiting a vanishing shear modulus. This is the case of pentamode materials, in which shear modulus is drastically smaller than bulk modulus [3]. Pentamode materials exhibit fluid-like properties and are often called metafluids. A proposed design is composed of beams with variable conical cross-sections with only their tips touching in a diamond type lattice [28]. In this design, any stress flowing through the lattice propagates through the tips of the cones [29]. As a result, the diameter of the cones has a minimal effect on the material's stiffness, while significantly influencing the mass density. Thus, the mass density of pentamode materials can be decoupled from their stiffness and be changed independently. Pentamode materials could be used to achieve acoustic cloaking (the equivalent of optical cloaking), by guiding mechanical waves in preferred directions inside the material [3].

In the thermodynamic formulation of materials' properties, the elasticity tensor, and by extension bulk and shear moduli, are defined as positive quantities, or else the material will be unstable. In the context of the theory of elasticity, a material with negative moduli can exist but cannot be stable if unconstrained [8]. However, if that material is constrained, stability can be achieved. This disagreement arises from assuming restrictions in the particles' internal degrees of freedom and the external fields exerted on them when the system is analyzed thermodynamically. Regardless, experimental evidence of negative moduli has been reported over the years. Foams hydrostatically compressed appeared to display a negative incremental bulk modulus (bulk modulus is the inverse of compressibility) due to buckling of its cells [30]. Various structures have been observed to expand in one or two directions under hydrostatic pressure [31–33]. This response is called negative linear or area compressibility, respectively. Negative bulk modulus materials could be used in the development of new actuators and protective mechanical devices [7] or the design of smart deployable space structures [34].

The aforementioned is closely related to the case of negative thermal expansion, where contractions in one or two directions occur as the system gets warmer [35]. Negative bulk modulus and negative thermal expansion are not identical, but it is hinted from experimental evidence that there is a correlation between them [36]. Negative thermal expansion is known to occur in the molecular level in certain framework structures, such as zeolites or metal oxides [35]. However, larger structures with this property have been fabricated [37,38]. Aerospace, electronics and high precision optical mirrors could benefit from the introduction of negative thermal expansion materials [35,36].

When a material is stressed, there is a restoring force, opposite to the stress, trying to return the system to its original state. This restoring force is proportional to the material's stiffness, which is a positive quantity for most systems. When stiffness is negative, this force assists the stress, instead of opposing it. Negative stiffness has been observed in structures which snap from one stable state to another while going through an unstable state in between. Examples of this can be traced in simple systems, like a buckled beam, or more complex configurations, such as the von Mises truss [39]. Negative stiffness structures can be included in composite materials to achieve stability, while benefiting from high damping properties due to these inclusions [40,41]. Negative stiffness devices can be exploited in building's infrastructure, as earthquake protection [42], and in vehicle seats, by isolating the driver from external vibrations [43].

When a material is compressed in one direction it is natural to expect it to expand in the other two, lateral, directions. This response is described as a positive Poisson's ratio and is common for most materials. Over the years, materials with a negative Poisson's ratio (*auxetics*) have been an increasingly investigated topic [10,44,45]. *Auxetics* have the counter-intuitive property of laterally compressing when compressed in one direction. Negative Poisson's ratio was reported for the first time in a foam material by Lakes in 1987, although the term '*auxetic*' was adopted later [11]. The *auxetic* behaviour of foams is due to the holes' walls protruding inward. Utilizing this re-entrant mechanism, *auxetic* behaviour can be achieved in isolated unit cells. There are plenty re-entrant designs that have been tested and result in a negative Poisson's ratio, such as the "bowtie" [46]. Most patterns are in 2D but can be expanded in 3D with various configurations. Chiral materials exhibit *auxetic* behaviour. When the 2D structure is stressed, the nodes turn and the ligaments bend resulting in a Poisson's ratio that could reach the value of -1 for a large range of strains [9]. Combining different type of patterns could result in composite materials with superior properties [47]. Rotating polygons is another type of 2D *metamaterials* that result in *auxetic* behaviour [48]. Negative Poisson's ratio is obtained from the rotation of the rigid units (polygons), joined with each other through hinges. Regardless of the type, *auxetic* materials exhibit high indentation resistance. During impact, the material is compressed laterally, becoming denser at the region of impact, which makes it harder to penetrate [49]. Furthermore, it has been shown that the energy of the impact is dissipated in the transverse directions, greatly reducing the peak stress at the bottom layers [50]. When an *auxetic* is stretched it expands in all directions. This can be traced down to the individual cells, which get bigger when the tensile stress is applied. When a crack is formed, the expansion of each cell will tend to close it, making *auxetic* materials resistant to fracturing [51]. As Poisson's ratio approaches the value of -1, shear modulus goes to infinite, which results in a high shear stiffness [52]. Thus, *auxetics* are eligible candidates for efficient and durable shock absorbers to be used in body protection equipment [50]. There are applications that arise directly from the negative Poisson's ratio. In common cellular materials for example, when the basic unit cell is stretched in one direction, it also compresses in the other two. As a result, the pore size does not increase homogeneously. In *auxetic* materials however, stretching in one direction results in stretching of the other two as well. This uniform size increase makes *auxetic* materials suitable for tunable filters [53]. Adding *auxetic* elements in piezoelectric sensors and actuators could potentially increase the accuracy of their movement [44]. Biomedical engineering could benefit from negative Poisson's ratio structures with *auxetic* stents. The blood flow inside arteries will expand the stent along its axis, which in turn results in an expansion in the lateral directions, opening up clogged blood vessels [54].

There is a plethora of additive manufacturing techniques available for the fabrication of *mechanical metamaterials*. Architecture is crucial, so the fabrication process should allow for a high degree of flexibility in the design. Additionally, the chosen method must have the appropriate resolution to fabricate structures in the length scale which corresponds to the size of the *metamaterial* and its features. Each technique uses different materials and as a result some of them may be prohibitive with regards to the intended application. 3D printing is widely used in the mm-cm scale for the ease of availability and the variety of materials which it can work with. The method uses a layer-by-layer approach to fabricate both 2D and 3D structures [50,55,56]. On the same scale, there is the alternative of casting methods, in which a mold is filled with a liquid that solidifies and adopts the form of the mold [57,58]. Depending on the material that is used, the solidification process differs i.e. temperature dependent or polymerization. Laser sintering [59,60] and laser ablation [53] are also options to consider. There are quite a few lithography techniques that can be utilized, such as inverted stereolithography or projection microstereolithography [56,61,62]. In this work, *multiphoton lithography (MPL)* was used for the fabrication of structures with features in the nm scale.

MPL is a well-established fabrication method [63] which has contributed in numerous fields over the years [64–66]. A pulsed IR laser is tightly focused inside the volume of a photocurable resin. Polymerization can occur only when two (or more) photons are absorbed. The strict conditions of multiphoton absorption can only be satisfied inside the focus volume of the laser beam. 3D in-depth fabrication is achieved by moving that focus volume inside the material. The pattern is provided by a computer, which also controls the entire process. *MPL* is an efficient and accurate method having a high degree of repeatability in its results. It can fabricate complex 3D structures in a one-step process with a resolution exceeding 100nm. For such reasons, *MPL* is an excellent candidate for manufacturing *mechanical metamaterials*. However, the purpose of *MPL* is two-fold; Apart from the advantages in the fabrication process, its exceptional resolution allows for design across multiple length scales. The latter is commonly known as structural hierarchy and can greatly affect the resulting properties of materials [67].

CHAPTER 1: VISCOELASTIC MATERIALS

This first chapter serves as an introduction to *viscoelastic* materials. The term *viscoelastic* is used to describe materials that, apart from an elastic response, also exhibit viscous behaviour under mechanical stress. The reason behind that is due to the existence of long molecules, which enable larger molecular allocations inside the material. Polymers fall under this category, so it is vital to be familiarized with the theory of *viscoelasticity* in order to study their mechanical properties. The chapter begins with the basic theory of elasticity which leads to the generalized Hooke's law for solids. Following that, the theory of *viscoelasticity* is presented, examining the two fundamental mechanisms of deformation. The chapter concludes with the mathematical model used to describe the mechanical response of the materials.

Hookean Solid: The displacement of a spring when subjected to an external force is given by Hooke's law,

$$F = -k * x, \text{ where}$$

- F: Force applied on a spring (N),
- k: Stiffness of the spring (N/m),
- x: Displacement of spring (m)

The classical theory of elasticity assumes that atomic bonds respond in the same manner as springs to external forces. Based on this model, Hooke's law can be modified to describe the mechanical behaviour of isotropic, homogeneous, linearly elastic materials which are subjected to small deformations. Force and displacement are replaced by stress and strain, respectively, and Hooke's law becomes,

$$\text{const.} = \frac{\sigma}{\epsilon}$$

Stress, σ , is the applied force on a surface measured in N/m^2 and strain, ϵ , is defined as the change in length over the original length. The constant is one of the elastic moduli (Young's, bulk or shear modulus) and depends on the direction and nature of the applied stress.

Elastic Moduli: The elastic properties of a material are characterized by a specific set of parameters. These parameters, referred to as elastic moduli, include Young's modulus E , shear modulus G and bulk modulus B . They connect the applied stresses with the resulting strains and are characteristic of each material. In continuum mechanics, more than one stresses are usually applied, and so second order tensors are used to describe a material's stress and strain. They are called Cauchy's tensors named after the French mathematician, engineer and physicist Augustin-Louis Cauchy.

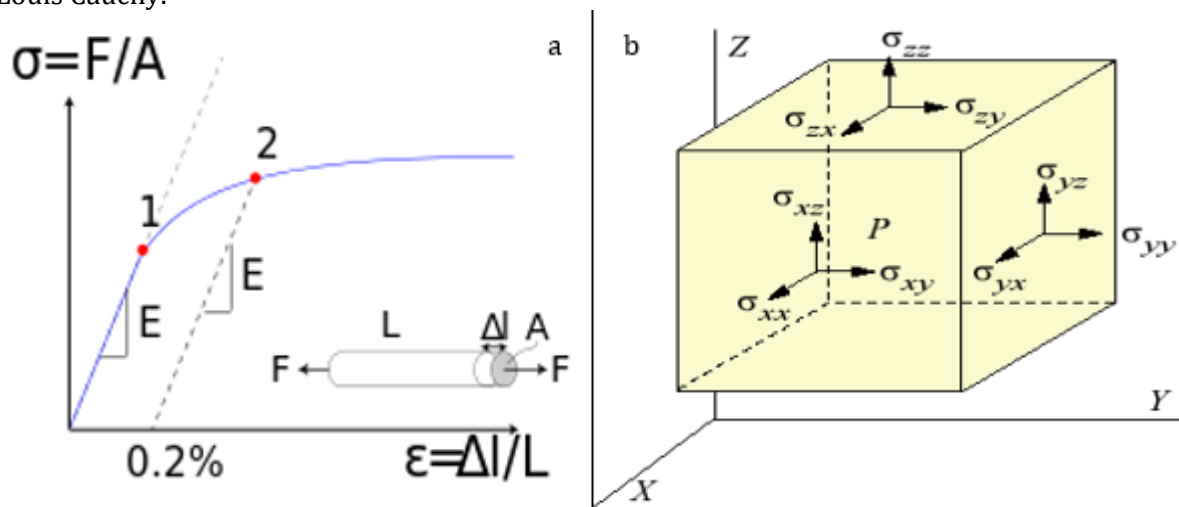


Figure 1-a) Strain-stress curve of nonferrous alloy [Wikipedia], and b) Normal and shear stresses on a cube [efunda.com].

Young's modulus, E , refers to deformations normal to the surface of the material (Figure 1-b). It is a measure of a material's stiffness. It can be determined through a tensile test, whose results are plotted in a stress-strain curve [68]. The response of each material is different, but a general behaviour can be observed. The tensile test of a nonferrous alloy is used as an example in Figure 1-a. At first, the material has a linear response to the applied load. This is called the elastic region and the slope of the curve is equal to the Young's modulus of this material. If the load vanishes while in the elastic region, the material will return to its original length. As the load increases, the material will either go into the plastic region and eventually fail or fail directly. Plastic deformation is characterized by a sudden increase in strain with a minor increase in stress. The relation between these two is no longer linear and the material is permanently deformed. Young's modulus, elastic/plastic deformation limits and failure mechanisms are but a few of the crucial information that can be extracted from a stress-strain curve [69].

When a force is applied parallel to surface (Figure 1-b), the material is subjected to shear stress. Shear modulus, G , is defined as the ratio of shear stress to shear strain and is used as a measurement for rigidity. During shear deformations the material changes shape under constant volume. For small deformations it can be shown that [70],

$$G = \frac{E}{2*(1+\nu)}, \text{ where } \nu: \text{Poisson's ratio} \quad (1)$$

Bulk modulus, B , is a measurement of how resistant a material is to uniform compression; the material's volume changes but it retains its shape. It is defined as the ratio of infinitesimal pressure increase to the relative volume decrease,

$$B = \frac{P}{\frac{\Delta V}{V_0}} = \frac{\frac{1}{3}*(\sigma_x + \sigma_y + \sigma_z)}{\varepsilon_x + \varepsilon_y + \varepsilon_z} \quad (2)$$

Mechanical stability requires the elastic moduli to be positive. However, this is a rule for unconstrained materials only. A constrained material with negative moduli can be stable. The boundaries in which a material is stable, as well as the various regimes of Poisson's ratio, are shown in Figure 2.

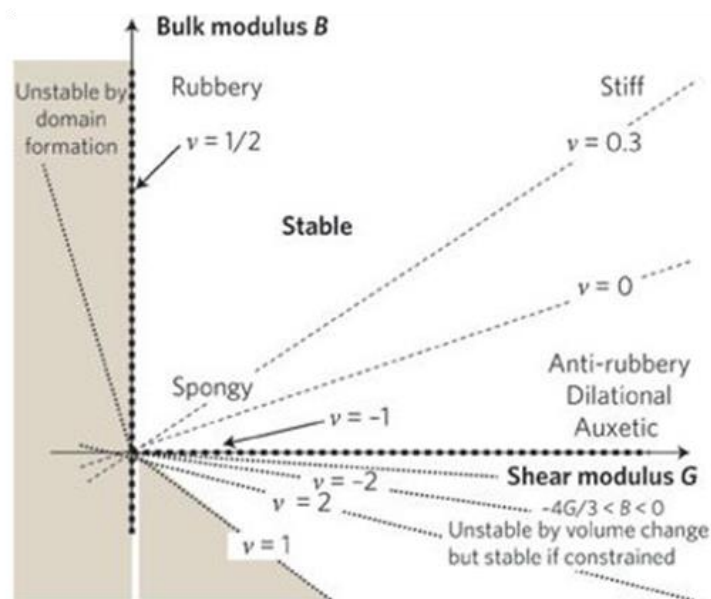


Figure 2- Stability map of materials [71].

Poisson's Ratio: When a material is compressed in one direction, it tends to expand in the other two, and vice versa. This intrinsic quality of most materials is called Poisson's ratio, ν . For small deformations, it is equal to the negative ratio of transverse, ε_T , to axial, ε , strain,

$$\nu = -\frac{\varepsilon_T}{\varepsilon}$$

In the context of positive moduli, Poisson's ratio can take values from -1 to 0.5. Most materials have a positive value of ν . There are some materials however that have the counter-intuitive behaviour of negative ν . They are called *auxetic* and when they are compressed in one direction, compression also occurs in the transverse plane.

Generalized Hooke's Law: Assume a material that is subjected to uniaxial stress along the x-axis, σ_x . It creates a normal strain along the x-axis which, for small deformations, is equal to $\varepsilon_x = \frac{\sigma_x}{E}$, as per Hooke's law. However, because of the compression on the x-axis, the material is stretched in the y and z directions. This is due to shear stresses, σ_T , which result to shear strains, ε_T : $\varepsilon_T = -\nu * \varepsilon_x \Rightarrow \varepsilon_T = -\nu * \frac{\sigma_x}{E}$. When uniaxial stresses are applied on all three axes, the resulting normal strains become,

$$\begin{aligned}\varepsilon_x &= \frac{\sigma_x}{E} - \frac{\nu}{E} * (\sigma_y + \sigma_z) \Rightarrow \varepsilon_x = \frac{1+\nu}{E} * \sigma_x - \frac{\nu}{E} * (\sigma_x + \sigma_y + \sigma_z) \\ \varepsilon_y &= \frac{\sigma_y}{E} - \frac{\nu}{E} * (\sigma_x + \sigma_z) \Rightarrow \varepsilon_y = \frac{1+\nu}{E} * \sigma_y - \frac{\nu}{E} * (\sigma_x + \sigma_y + \sigma_z) \quad (3) \\ \varepsilon_z &= \frac{\sigma_z}{E} - \frac{\nu}{E} * (\sigma_x + \sigma_y) \Rightarrow \varepsilon_z = \frac{1+\nu}{E} * \sigma_z - \frac{\nu}{E} * (\sigma_x + \sigma_y + \sigma_z)\end{aligned}$$

Switching to matrix notation, the above can be summarized in the following,

$$\mathcal{E} = \frac{1+\nu}{E} * T - \frac{\nu}{E} * tr(T) * I, \text{ where} \quad (4)$$

$$\begin{array}{ccc} \varepsilon_{xx} & \varepsilon_{xy} & \varepsilon_{xz} \\ \mathcal{E} = \varepsilon_{yx} & \varepsilon_{yy} & \varepsilon_{yz} : \text{Strain matrix,} \\ \varepsilon_{zx} & \varepsilon_{zy} & \varepsilon_{zz} \end{array} \quad \begin{array}{ccc} \sigma_{xx} & \sigma_{xy} & \sigma_{xz} \\ T = \sigma_{yx} & \sigma_{yy} & \sigma_{yz} : \text{Stress matrix,} \\ \sigma_{zx} & \sigma_{zy} & \sigma_{zz} \end{array}$$

$tr(A) = a_{11} + a_{22} + a_{33}$: Trace of matrix A, I : unit matrix

By adding the left side of equations (3) and messing with equation (4) we get,

$$tr(\mathcal{E}) = \frac{tr(T)}{E} - \frac{2*\nu}{E} * tr(T) \Rightarrow tr(\mathcal{E}) = \frac{1-2*\nu}{E} * tr(T) \quad (5)$$

$$T = \frac{E}{1+\nu} * \left\{ \mathcal{E} + \frac{\nu}{E} * tr(T) * I \right\} \quad (6)$$

Substituting (5) to (6) results in,

$$T = \frac{E}{1+\nu} * \left\{ \mathcal{E} + \frac{\nu}{1-2*\nu} * tr(\mathcal{E}) * I \right\} \Rightarrow T = \frac{E}{1+\nu} * \mathcal{E} + \frac{E*\nu}{(1+\nu)*(1-2*\nu)} * tr(\mathcal{E}) * I \quad (7)$$

Equation (7) is known as the generalized Hooke's law which connects the applied stresses with the resulting strains of a solid. Normal stresses result in normal strains and shear stresses result in shear strains,

$$\begin{aligned}T_{ii} &= \frac{E}{1+\nu} * \varepsilon_{ii} + \frac{E*\nu}{(1+\nu)*(1-2*\nu)} * tr(\mathcal{E}) * I \\ T_{ij} &= \frac{E}{1+\nu} * \varepsilon_{ij} = 2 * G * \varepsilon_{ij} \quad (8)\end{aligned}$$

From equations (2) and (5), bulk modulus becomes,

$$B = \frac{\frac{1}{3} * tr(T)}{tr(\mathcal{E})} = \frac{\frac{1}{3}}{\frac{1-2*\nu}{E}} \Rightarrow B = \frac{E}{3*(1-2*\nu)} \quad (9)$$

Using equations (1) and (9) it can be shown that,

$$\frac{E*\nu}{(1+\nu)*(1-2*\nu)} = \frac{E}{3*(1-2*\nu)} + \frac{E}{3*(1+\nu)} = B - \frac{2}{3} * G \equiv \lambda$$

Finally, equation (7) is simplified to,

$$T = 2 * G * \mathcal{E} + \lambda * tr(\mathcal{E}) * I \quad [10]$$

In equation (10), G and λ are called Lamme constants. The parameter λ does not have any physical interpretation.

Viscoelasticity: When a material is stressed, the lengths and angles of molecular bonds may distort, slightly moving atoms to new positions of greater internal energy. This response occurs almost instantly, at around $\sim 10^{-12}$ s and is described by the theory of elasticity. However, polymers display another, fundamentally different, deformation mechanism. Because the tightly packed formation of crystalline structures is not present here, larger-scale rearrangements of the atoms may occur when an external stress is applied. The amorphous inorganic network of atoms in a polymer has sufficient molecular mobility for such movements. Molecular mobility depends on physical and chemical factors [72]. It is not a homogeneous quantity throughout the polymer and varies locally. These movements are not instantaneous and as a result depend on the duration of the applied stress. Materials that display this kind of response are characterized by a viscous behaviour. The first and second laws of thermodynamics state that a mechanical work, $F*dx$, done on the system produces an increase in its internal energy, dU , and a decrease in entropy, dS :

$$F * dx = dU - T * dS$$

Let us take the example of a rubber band [73]. The unstressed rubber band is a macrostate, with all the different combinations of molecules' position and orientation resulting in an unstressed rubber band be the microstates of the system. The stretched rubber band is another macrostate of the system. When the rubber band is stretched, its molecules begin to align in the direction of the strain, reducing the number of the microstates of the system, and thus the entropy of the system is reduced too. Since this process is non-spontaneous (no unstretched rubber band will become stretched without an external force), heat flows outside of the system to its surroundings. When the stretching force is released, the rubber band returns to an unstretched state. The molecules go back to their random positions and, since the number of microstates is increased, the entropy of the system is increased as well. All stretched rubber bands will return to an unstretched state as soon as the stress is released. Thus, this process is spontaneous, which means that heat flows into the system from its surroundings. This also works the other way around: The force needed to keep a rubber band at fixed elongation increases as heat flows into the rubber band, which will increase its temperature. This behaviour is the opposite of energetic elasticity, which stems from thermal expansion. Knowing which deformation mechanism is dominant, is a crucial part in determining a material's mechanical response. It is apparent from the above equation that the importance of the entropic contribution increases with temperature. This can be used to determine whether the nature of a material's stiffness is energetic or entropic. Materials which display both viscous fluidity and elastic solidity are called *viscoelastic*.

Mechanical characterization tests of *viscoelastic* materials are similar to the uniaxial tensile tests used on elastic solids. Time dependency of stress and strain in elastic solids is mostly insignificant, so, when *viscoelastic* materials are considered, the measurements need to be modified, as to

include this time dependency. The most common of these tests are creep, stress relaxation and dynamic loading. In creep tests, a steady uniaxial stress σ_0 is applied and the time dependent strain $\varepsilon(t)$ is measured, as seen in Figure 3-a. Upon loading, the material strains immediately to some extent, as the result of elastic deformation due to bond distortion. As time progresses, the material continues to deform due to molecular movement, until it reaches an equilibrium. The inverse procedure is called stress relaxation (Figure 3-b). The material is kept at a steady strain ε_0 and the time-varying stress $\sigma(t)$ is recorded. An immediate decrease in stress is observed due to bond distortion, followed by a continuous relaxation due to the molecular mobility, until stress reaches a constant value. Creep and stress relaxation tests are both manifestations of the same mechanisms. Even though parallels can be made at the time limits of the curve (near $t=0$ and the final equilibrium), one test cannot be extracted from the other. In particular, the relaxation response, in general, moves towards equilibrium faster than the creep response.

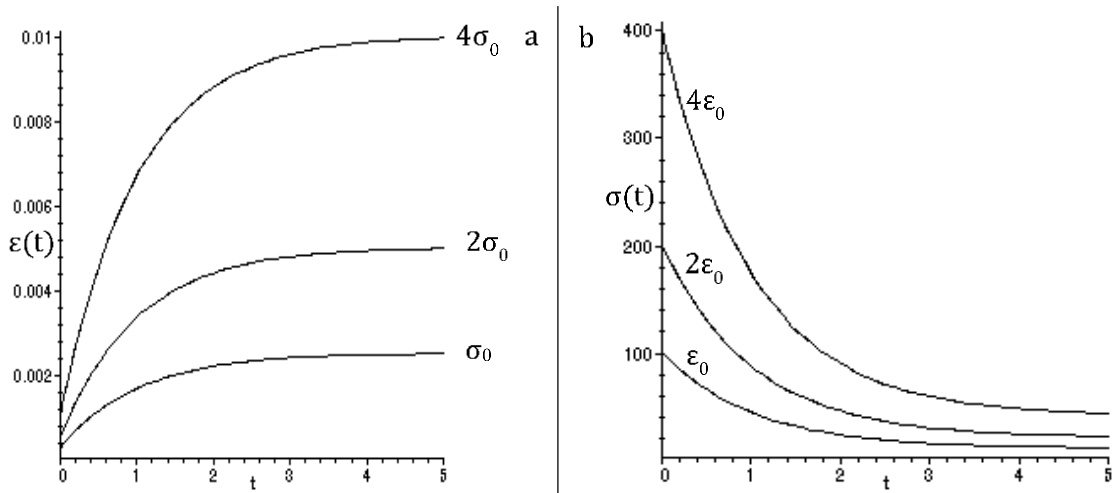


Figure 3-a) Typical results of a creep test, and b) Typical results of a stress relaxation test [74].

Creep and stress relaxation tests provide accurate information for the long-time (minutes to days) response of a material, but for the short-time (seconds or less) response another method is required. In dynamic tests, a sinusoidal stress is applied on the material and the resulting strain is measured. *Viscoelastic* materials will eventually reach a steady state in which strain is also sinusoidal, having the same angular frequency as the stress. However, the strain is delayed in phase by an angle δ , in analogy with the delayed strain in creep tests. Strain and stress can be expressed as,

$$\varepsilon(t) = \varepsilon_0 * \cos \omega t$$

$$\sigma(t) = \sigma_0 * \cos(\omega t + \delta)$$

It is convenient to write stress as a complex quantity whose real and imaginary parts are, respectively, in and out of phase with the strain (Figure 4),

$$\sigma^* = \sigma'_0 * \cos(\omega t) + i * \sigma''_0 * \sin(\omega t)$$

By projecting stress and strain in the complex plane, useful information can be attained,

$$\sigma'_0 = \sigma_0 * \cos \delta \Rightarrow E' = \frac{\sigma'_0}{\varepsilon_0}$$

$$\sigma''_0 = \sigma_0 * \sin \delta \Rightarrow E'' = \frac{\sigma''_0}{\varepsilon_0}$$

$$\tan \delta = \frac{E''}{E'}$$

The amplitudes σ'_0 and σ''_0 can be used to define two different dynamic moduli. The storage modulus E' is the ratio of the in-phase stress to strain and represents the elastic portion of the material's response. It is a measure of the stored energy due to bond distortion. The loss modulus E'' is the ratio of the out-of-phase stress to strain and represents the viscous portion of the material's response. It is a measure of the energy dissipated as heat due to molecular movement. The value of $\tan \delta$ determines if the material's response is elastic (bond distortion) or viscous (molecular movement) in origin. If $\delta = 0^\circ$ the material is purely elastic while if $\delta = 90^\circ$ the material is defined as purely viscous (plastic).

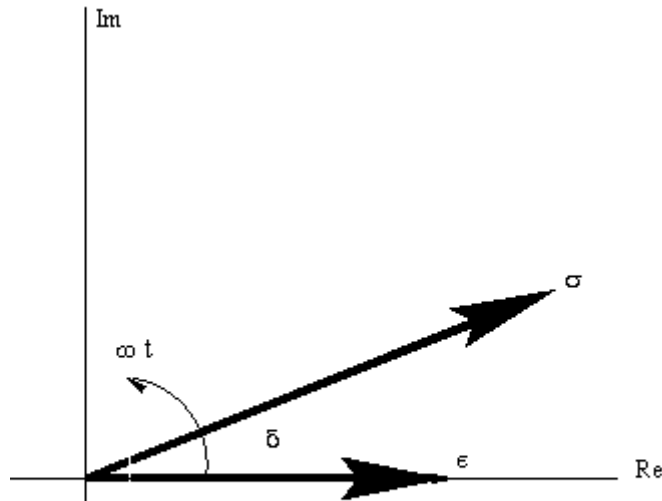


Figure 4- Representation of stress and strain vectors in the complex plane [74].

Kelvin-Voigt Model: A viscoelastic material can be described by a simple model of only two components. A Hookean spring represents the instantaneous response of the elastic behaviour, while the time-dependent viscous behaviour is represented by a Newtonian dashpot. If k is the spring constant (N/m^2) and η is viscosity of the dashpot ($N*s/m^2$),

$$\sigma = k * \varepsilon, \text{ Spring}$$

$$\sigma = \eta * \frac{\partial \varepsilon}{\partial t} = \eta * \dot{\varepsilon}, \text{ Dashpot}$$

The format where a dashpot and a spring are connected in parallel is called the Kelvin-Voigt model (Figure 5). In this arrangement, strain is the same in all parallel components, while the total stress is the sum of all component's stress,

$$\varepsilon_T = \varepsilon_{spr} = \varepsilon_{dash}$$

$$\sigma_T = \sigma_{spr} + \sigma_{dash} = k * \varepsilon + \eta * \dot{\varepsilon}$$

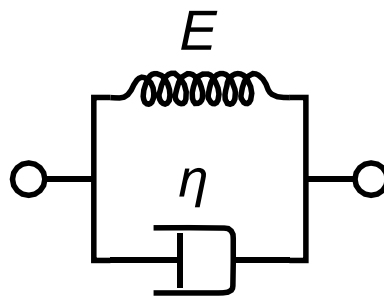


Figure 5- Kelvin-Voigt model representation [wikipedia].

CHAPTER 2: MULTIPHOTON LITHOGRAPHY

On this chapter, *Multiphoton Lithography* is decomposed to its basic principles and the required conditions under which it can occur are examined. Initially, the fundamental physics of multiphoton absorption and Abbe's diffraction limit are analyzed before the method itself is explicated.

Multiphoton Absorption: As the name suggests, *MPL* is based on the non-linear optical effect of multiphoton absorption. Non-linear optics include all phenomena where the dielectric polarization P of a material and the electric field E of an electromagnetic wave are not linearly related [75]. This is due to the appearance of higher-order field terms,

$$P = \epsilon_0 * (\chi^{(1)} * E + \chi^{(2)} * E * E + \chi^{(3)} * E * E * E + \dots), \text{ where}$$

ϵ_0 : Vacuum permittivity,

$\chi^{(1)}, \chi^{(2)}, \chi^{(3)} \dots$: First-, second- and third- order optical susceptibilities

The power in which E is raised represents the number of transitions that take place. Namely, the first term describes linear effects, such as the absorption or emission of one photon, while all other terms are used to describe phenomena in the non-linear regime. For example, the second term is linked with the mechanisms of second harmonic generation. The occurrence of a n^{th} -order effect depends on the n^{th} power of the radiation intensity, and as a result, non-linear phenomena require high intensities for their occurrence. Due to the ever-increasing use of lasers, higher field intensities can be obtained, which make non-linear effects easier to observe and study. However, high intensity is not the only requirement for such exotic effects, and this will be made apparent in the following case of *two-photon absorption (TPA)*.

An electron has a non-zero probability to transition from an energy state A to a higher energy state B, when a photon of equal or higher energy compared to the energy difference between states A and B is absorbed. This transition can also occur with the absorption of multiple photons, presenting, however, a significantly lower probability. In the case where two photons induce this excitation, the phenomenon is called two photo absorption. Since *TPA* consists of two transitions, it is classified as a second order non-linear effect and its probability of occurring depends on the square of the radiation intensity. Two mechanisms of *TPA* can be distinguished: sequential and simultaneous absorption (Figure 6).

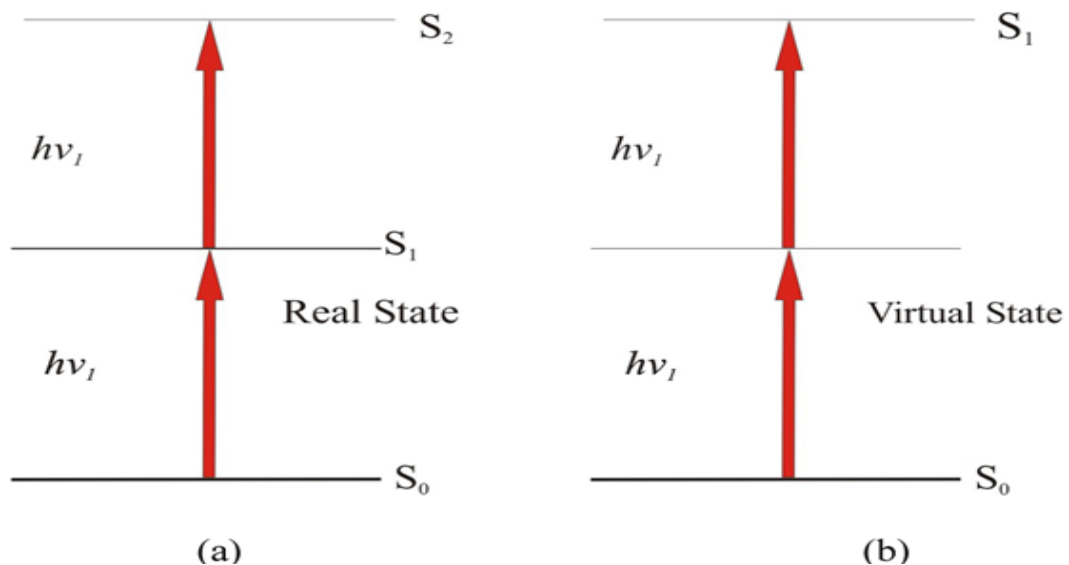


Figure 6- (a) Sequential absorption of two photons, and (b) Simultaneous absorption of two photons [63].

Assume a molecule or atom that is irradiated with photons of energy $h\nu_1$. The time interval between the absorption of the first and the second photon is $\Delta\tau$. In sequential absorption (Figure 6-a), the electron is excited from the fundamental energy state S_0 to a real intermediate energy state S_1 by absorbing one photon of energy $h\nu_1$. If $\Delta\tau$ is smaller than the lifetime of S_1 , a second photon, with the same energy of $h\nu_1$, is absorbed before the electron returns to S_0 . Thus, the electron is excited to the energy state S_2 . Since the intermediate state S_1 is a real energy level, the atom/molecule can absorb in the respective wavelength of the energy $h\nu_1$, regardless if *TPA* occurs or not. The lifetime of an electron in a real energy state is 10^{-9} - 10^{-4} sec. But what if there is no intermediate state between S_0 and S_2 ? Can the $S_0 \rightarrow S_2$ transition occur then? The answer is yes, and this is the case of simultaneous absorption (Figure 6-b). Since S_1 does not exist, the atom/molecule does not absorb photons of energy $h\nu_1$. However, an electron can be excited to S_2 by *TPA* through a virtual state. The virtual state has a much shorter lifetime, in the order of $\sim 10^{-15}$ sec. In the same manner, if $\Delta\tau$ is smaller than this lifetime, the second photon will be absorbed, and the electron is excited to S_2 . It is apparent that except high field intensities, a small $\Delta\tau$ is necessary as well. *MPL* is based on *two-photon polymerization (2PP)*, which, is the result of the simultaneous absorption mechanism of *TPA*.

Abbe's Diffraction Limit: Every optical imaging system can be limited by experimental factors, such as alignment errors or imperfections in its optical components. However, there is a fundamental limit for the maximum resolution every optical imaging system can achieve. It is called Abbe's diffraction limit and is due to the diffraction of light [76]. Focusing light inside a medium creates a spot of radius,

$$d = \frac{\lambda}{2 \cdot n \cdot \sin\theta} \text{ where,}$$

λ : Wavelength of light (nm),

n : Diffraction coefficient of medium,

θ : Angle of convergence

The product $n \cdot \sin\theta$ is the numerical aperture (NA), and, in modern optics, ranges from 1.4-1.6. For the visible spectrum (400-700nm), the focusing spot ranges from 0.14-0.25 μ m. Reducing the wavelength would lead to a higher resolution, but also increase the risk of destroying the sample. The main advantage of *MPL* is that it can reach a greater resolution than the one Abbe's diffraction limit defines [77].

Multiphoton Lithography: *MPL* is a direct laser writing technique based on *2PP* that allows the fabrication of high-resolution 3D structures up to the nm scale[78]. The required conditions for *2PP* are provided by a pulsed femtosecond laser, tightly focused inside a photosensitive material. The process is accurately controlled with computer software (Computer Aided Design; CAD), which scan the material with the laser beam to create the desired pattern. Laser and material movement is controlled with mirrors and linear stages, respectively. The main aspect of *MPL* is its ability to create 3D structures in a one-step process. Other lithography methods do not have that advantage. In one-photon polymerization for example, the material is polymerized wherever it is irradiated. This is not the case for *2PP*, since the material does not absorb in the laser wavelength, as seen in Figure 7. Instead, polymerization occurs only inside the focus volume where the radiation intensity is large enough to trigger *TPA*. The minimum pulse fluence at which *2PP* occurs is called the polymerization threshold fluence and for a typical *MPL* material is in the order of J/cm². Pulse width is of utmost importance. Femtosecond pulses have a high peak power, reducing the polymerization threshold fluence and enabling *TPA* lower energy values. Additionally, at ultra-short laser pulses material's temperature rise due to laser heating becomes less important. Thus, thermal damage done on the material is minimized and temperature-

dependent radical diffusion is restricted considerably. All these factors contribute to the resolution, which has been shown to reduce as laser pulse width is reduced [79].

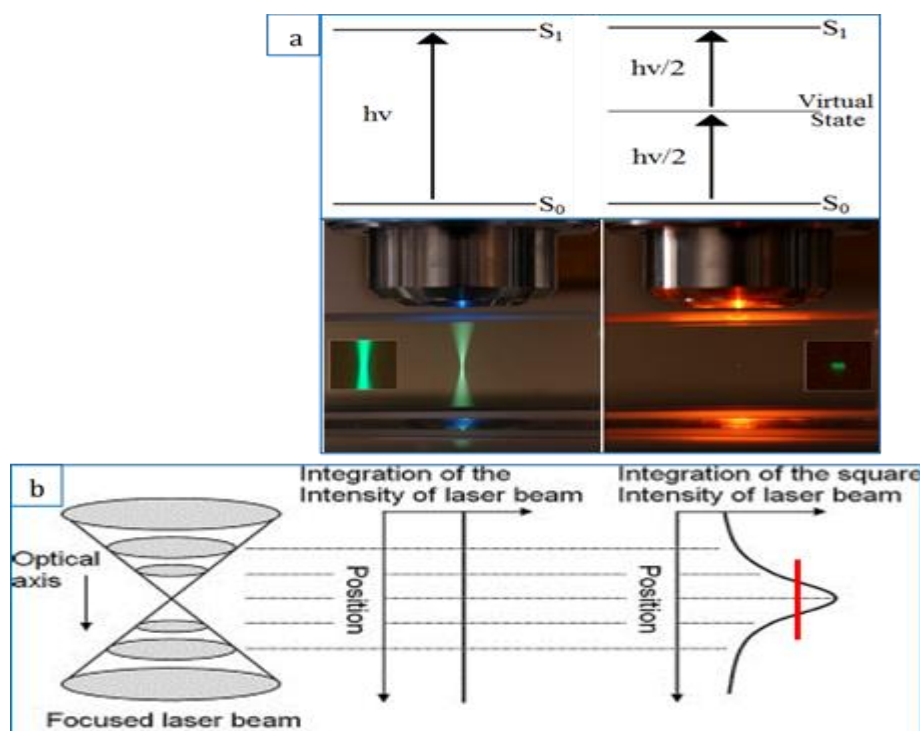


Figure 7- a) Comparison of one-photon and two-photon polymerization. Green colour indicates polymerization [Steve Ruzin and Holly Aaron, UC Berkeley], and b) Comparison of one-photon and two-photon absorption with respect to the optical axis. The red line is the energy threshold [66].

The focus volume is defined by Abbe's diffraction limit. Due to the square dependence of the intensity, polymerization occurs only in a portion of it, called voxel. That way, the fundamental diffraction limit is by-passed, and higher resolution is achieved. The movement of the focus volume, and therefore the voxel, is controlled with computer software, which allows for 3D in-depth fabrication inside the material. Voxel shape is typically that of an ellipsoid but can be made spherical with the right experimental conditions [80]. Apart from the effect of pulse width on the voxel, its size can be controlled with other means as well. One way is by balancing between the photoinitiator concentration and the termination processes during the material's synthesis, which is a topic considered in the next chapter. A more direct way for voxel size control is with the energy and scanning speed of the laser pulses inside the material.

The voxel is the result of the material exposed to the laser beam. If this exposure changes, the size of the voxel is affected. Since the laser is mostly monochromatic, an increase in pulse energy results in a higher photon count per pulse, which in turn raises the probability of two photons being absorbed. More excited electrons lead to an enhanced polymerization and, consequentially, increase the voxel size. On the other hand, reducing the pulse energy leads to a weaker polymerization, until it stops at energy values lower than the energy threshold. The exposure is also affected by the scanning speed of the laser beam in the material. Higher scanning speeds mean that a reduced number of photons are incident on the same volume of material. This results in a lower polymerization, which makes the voxel smaller. Conversely, lower scanning speeds cause a larger voxel. In general, it can be said that voxel size is proportional to the pulse energy and inversely proportional to the scanning speed. Smaller voxel translates to higher resolution, so, ideally, the voxel needs to be as small as possible. An investigation of the energy and scanning speed is required for each material and every structure. This 'calibration' provides the ideal fabrication conditions of energy and scanning speed.

CHAPTER 3: HYBRID MATERIALS

The third chapter's focus is about the hybrid material used in *Multiphoton Lithography*. This analysis follows every step of the *sol-gel method*, which is used for its synthesis. Throughout this process, different molecules react with each other to form a homogenous and isotropic medium. The chemical compounds used, as well as the reactions that occur between them, are included in this section.

MPL materials: In order to be suitable for use in *MPL*, the material needs to possess a few particular properties. First and foremost, since *2PP* is the fundamental aspect of *MPL*, a high *TPA* cross-section is required. *2PP* occurs only inside the focal volume, where the high-intensity and short-duration pulses of the laser can lead to an increased *TPA* probability. Secondly, the material needs to be transparent to the wavelength of the laser source. If that were not the case, polymerization due to linear absorption would occur wherever the material was irradiated. This would create a handful of drawbacks. Since polymerization is not contained inside the focal volume, in-depth fabrication of structures in a one-step process would not be possible, while a decrease in resolution would be unavoidable and the average size of microstructures would not be able to go as low as the nm scale. Ideally, since an 800nm laser is used, the material needs to absorb strongly at 400nm and almost to nothing at 800nm, so polymerization can commence only if two photons, or more, are absorbed. Finally, structures fabricated with this material need to have a mechanical endurance, so that they can maintain the intended shape and not collapse after the fabrication process. Structure stability is a crucial factor, especially when one considers applications in photonics or mechanics.

Hybrid materials: The material we use is a hybrid material mainly consisting of the organic monomer compounds *3-(Trimethoxysilyl) propyl methacrylate* (MAPTMS) and *2-(Dimethylamino)ethyl methacrylate* (DMAEMA), which can be polymerized. These compounds have a weak absorption from IR to UV and a low *TPA* cross-section. Even though the material is made transparent to the laser source of 800nm, the *TPA* efficiency is poor. Polymerization can occur in higher energy values, but the material may be destroyed in the process. The number of decomposed molecules for every absorbed photon is called quantum yield. Monomers have, on average, a poor quantum yield. For such reasons, *4,4'-Bis(diethylamino) benzophenone* (Bis), which has a much higher quantum yield, is added to the mixture. Bis is a photoinitiator that absorbs strongly at 400nm but poorly at 800nm. It has a high *TPA* cross-section and is completely soluble in the solution. The addition of Bis makes *2PP* more efficient in lower energy values, while constraining polymerization in the focal volume. The problem of mechanical stability is solved with Zirconium Propoxide (ZPO), which ensures that Zirconium atoms are present in the fabricated structures, thus making them more durable. The UV-VIS transmission spectrum of the hybrid material is shown in Figure 8.

Sol-gel method: A sol is a colloidal suspension of solid particles in a liquid. Gravitational forces are negligible, thus interactions between molecules are determined by short-range forces, such as van der Waals attraction and surface charges. The system in this state is described by Brownian motion. Sol-gel process, as the name implies, involves the formation of a sol and its transformation to a gel. This method is widely used for the preparation of ceramic materials. The sol-gel method consists of two separate reactions: Hydrolysis and Condensation [63]. Both reactions are affected by a variety of factors which include the presence of a catalyst, its nature and concentration, pH and temperature [81]. The reactions that occur in the general case are presented in Figure 9.

Hydrolysis is the reaction of an organic monomer with a water molecule, typically under the presence of an acidic or basic solvent. The monomer is a silicon composite, where the R groups are carbon chains. A hydrogen atom replaces the R group of a monomer and an alcohol molecule is produced. Through condensation, monomers react with each other, forming a large inorganic network. If both reacting monomers are hydrolyzed, a water molecule is produced, and the reaction is called water condensation. If only one monomer is hydrolyzed, an alcohol molecule is produced, and this is the case of alcohol condensation. The ever-increasing water and alcohol concentrations eventually “clog” the system, slowing down the condensation process. By drying at low temperature or low pressure, the trapped water and alcohol molecules, as well as the solvent, are removed from the system and the condensation continues. This is called gelation and any significant volume loss occurs on this stage.

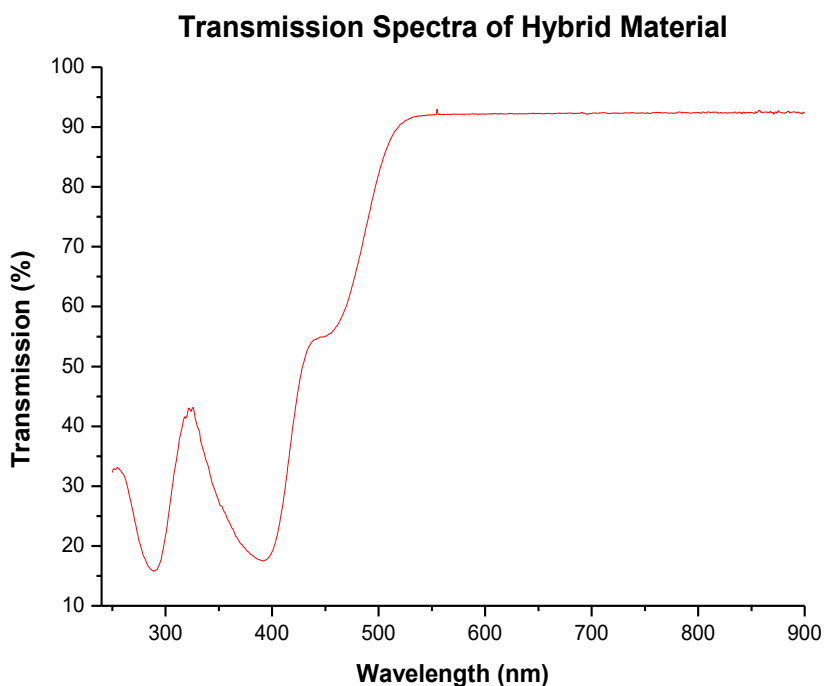


Figure 8- UV-VIS transmission spectrum of DMAEMA 10%.



Figure 9- Hydrolysis and condensation reactions in the general case of sol-gel method [81].

Material synthesis: The process in which the material is produced can be divided in four steps. Firstly, MAPTMS and 0.1M of HCl (diluted in water) are poured with a pipette in a glass flask. The processes of hydrolysis and condensation commence as soon as the two components are mixed. The solution is stirred for ~15mins to become homogeneous.

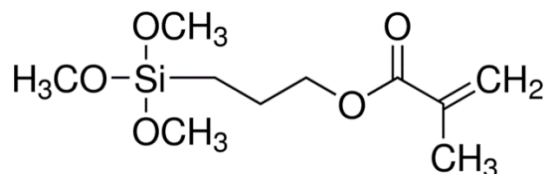


Figure 10- Structural formula of MAPTMS [SigmaAldrich]

Secondly, DMAEMA and ZPO (diluted in 70%w/w concentration of propanol) are poured with a pipette in a second flask. ZPO is extremely sensitive to moisture, so its contact with atmospheric air must be minimized. DMAEMA serves as a carrier for ZPO and no reactions occur between them. Again, the solution is stirred for ~15mins to become homogeneous.

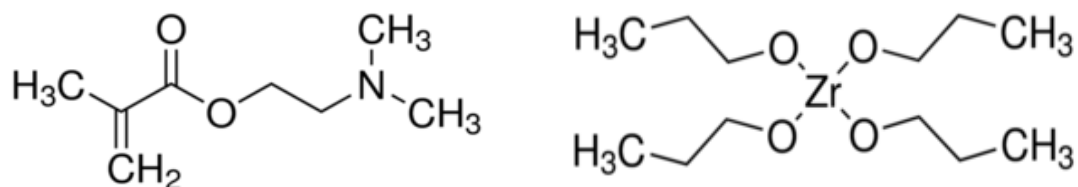


Figure 11- Structural formula of DMAEMA (left) and ZPO (right) [SigmaAldrich].

Then, the MAPTMS solution is poured in the DMAEMA-ZPO mixture. Zirconium atoms join the inorganic network of silicone, while the solution is stirred for ~15mins. During this stage, distilled water is added. The water molecules function as preservatives for the material. Finally, Bis is added at 1w% with respect to the mass of the monomers, and the mixture is stirred for ~15min one last time to ensure homogeneity. Bis does not have any reaction in the solution until the material is polymerized.

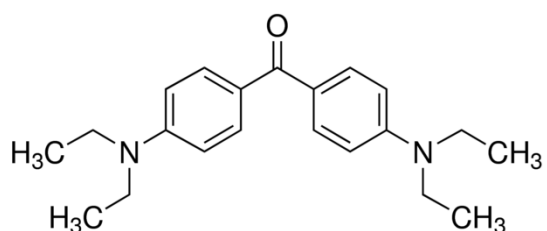


Figure 12-Structural form of Bis [SigmaAldrich].

Finally, the solution goes through a filtering process, in which molecules larger than 0.22µm are filtered out. These large molecules come from the formation of the inorganic network and can affect the fabrication process. After filtering, the now-complete material is stored in the fridge.

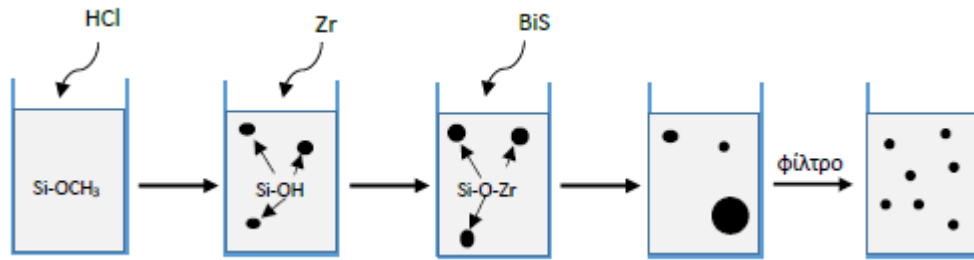


Figure 13- Production of the hybrid material.

The following table presents each component's mass and volume for 3ml of material. Also, the relations between the components are given under the table. These theoretical values were approached either with a high accuracy weight scale or with the appropriate pipette.

Table 1

	Molecular weight (gr/mol)	Density (gr/mL)	Mass (gr)	Volume (mL)
MAPTMS	248.35	1.045	1.6417	1.571
HCl	36.46	-	0.1426	-
DMAEMA	157.21	0.933	0.1484	0.159
ZPO	327.57	1.044	0.9280	0.889
H ₂ O	18.01	1	-	0.2
Bis	324.46	-	0.0267255	-

$$\frac{n_{ZPO}}{n_{MAPTMS}} = \frac{3}{7}, \quad \frac{n_{DMAEMA}}{n_{ZPO} + n_{MAPTMS}} = 10\%, \quad V_{total} = V_{ZPO} + V_{MAPTMS} + V_{DMAEMA}$$

Where n is the concentration of each component measured in mol. By deciding on the total volume of material, each component's mass and volume can be determined. The molecular mass and density of each component are needed for this calculation.

Sample treatment: Samples are created by casting a drop of material on a glass substrate. This glass substrate has undergone a specific treatment, so fabricated structures can attach on the surface of glass during *MPL*. This is accomplished by attaching MAPTMS on the glass's surface. First, the substrates are cleaned by being immersed in ethanol for 1 hour in the ultrasound machine. Then, the substrates are placed in a 20ml dichloromethane + 250μL of MAPTMS solution in the ultrasound machine for 4 hours. As a result, MAPTMS chains are added on the surface of the glass. The substrates are cleaned again with ethanol for 1 hour in the ultrasounds and, finally, they are stored in ethanol, ready for use. After a drop is casted on the substrate, the sample is placed under low vacuum conditions overnight, resulting in the gelation of the sol. The sample is ready for polymerization, but it can be preserved for several days under low vacuum conditions.

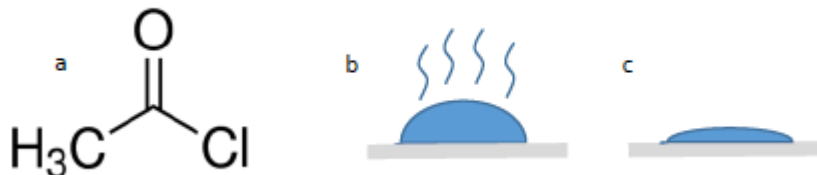


Figure 14- a) Structural form of dichloromethane [SigmaAldrich], b) Drop of material on glass substrate, and gelation, c) Dried sample.

The photopolymerization mechanism in *MPL* begins when the photoinitiator is excited and then decomposed, by absorbing two photons. This results in the production of initiating species of radicals which react with surrounding monomer compounds. The photoproducted radicals break the double bond between carbon atoms in DMAEMA and MAPTMS molecules. The produced radical monomers react with more monomer molecules, propagating and creating large polymer chains. When a polymer chain meets another chain or a photoproducted species of radical, the propagation ends. The termination of polymerization can also occur due to natural quenchers, such as oxygen molecules. The concentration and nature of quenchers in the material is a crucial factor, since they determine how far polymerization will propagate [66,82]. This mechanism can be summarized by the initiation, propagation and termination processes in the following table.

Table 2

Polymerization steps	Chemical reactions
Initiation	$I \xrightarrow{h\nu, h\nu} I^* \rightarrow \dot{R}$
Propagation	$\dot{R} + M \rightarrow R\dot{M} \xrightarrow{M} RMM \dots \rightarrow R\dot{M}_n$
Termination	$R\dot{M}_n + R\dot{M}_m \rightarrow RM_{n+m}R$ $R\dot{M}_n + \dot{R} \rightarrow RM_nR$

After polymerization, the samples are immersed for ~15min in a solution of 2-propanol: 1-propanol with a 7:3 mixture ratio, respectively. This process is called development and removes the unpolymerized material from the sample. Finally, the sample is washed with a solution of 2:propanol for ~15mins.

CHAPTER 4: EXPERIMENTAL SETUP

The setup of *Multiphoton Lithography* is reviewed, from the laser employed to all the different optical elements that constitute it. Additionally, the *nano-Dynamic Mechanical Analysis* technique is explicated.

Multiphoton Lithography: The irradiation source is a Ti:Sapphire pulsed fs laser, operating at 800nm. Pulse duration is less than 200fs with a repetition rate of 50-80MHz. A beam splitter divides the laser beam 70:30 between two experimental set-ups, Galvo-scanner and Nano-cube respectively. The two systems have two major differences. Galvo-scanner utilizes a galvanometric mirrors system (Scanlabs Hurryscan II) that scans the laser beam in the xy plane during fabrication. Scanning in the z-axis and larger scale xy plane movements were possible with a high-precision three-axis linear translation stage (Physik Instrumente M-500, 0.1 μ m minimum incremental motion). The tight focusing conditions of multiphoton absorption are provided by a focusing microscope objective lens with high numerical aperture (40x, NA=0.95, Zeiss, Plan Apochromat). This set-up can fabricate structures from a few decade μ m to even the mm scale. However, resolution is limited by the fact that the laser beam is constantly shifting during fabrication. This may not be a problem for large structures, it certainly is for smaller ones. Nano-cube on the other hand, has the laser beam on a fixed position, and all xyz-axis movements are performed by the sample through three piezoelectric stages (Physik Instrumente M-110.1DG, 50nm minimum incremental motion). Also, a different microscope objective is used (100x, NA=1.4, Zeiss, Plan Apochromat, oil immersed). Since the laser beam does not suffer any major deformations during fabrication, the resolution limitations that galvo-scanner has are not present here. Hence, a high spatial resolution in the order of a few nm can be reached. The size of the structures can go as low as a few decades nm.

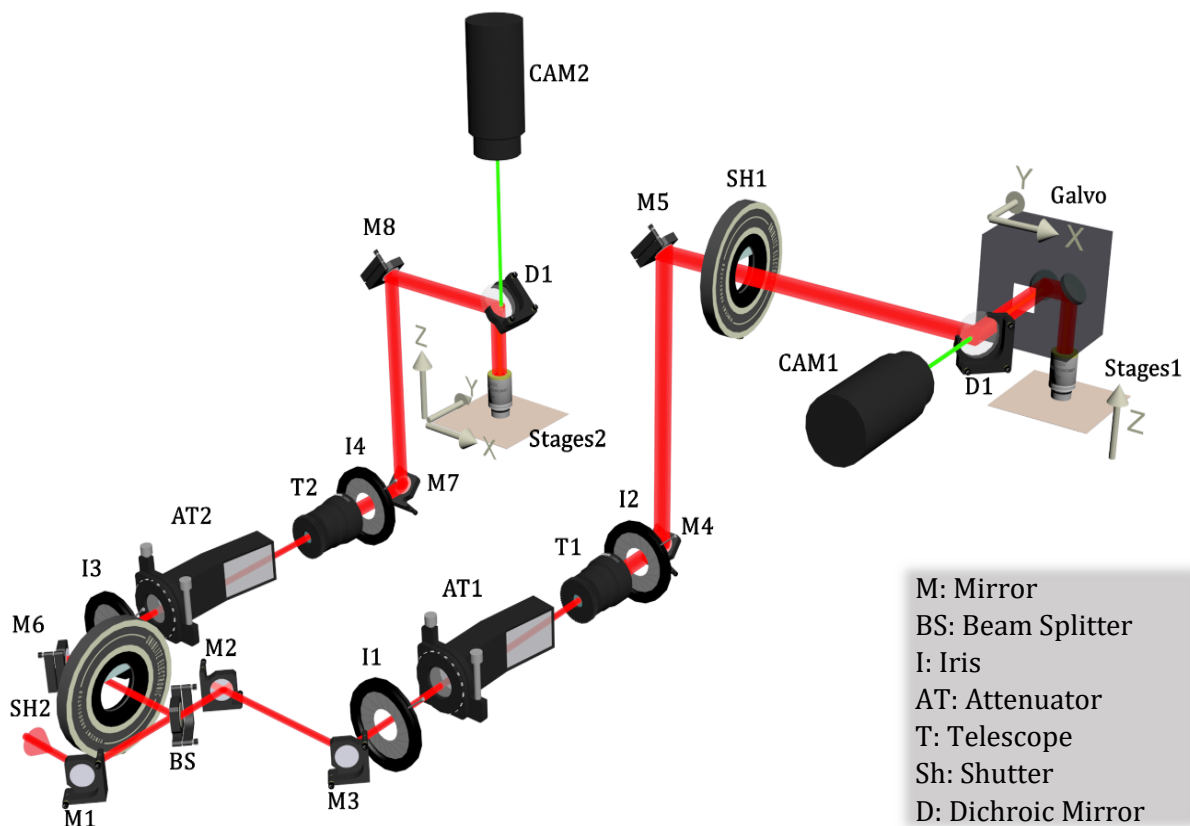


Figure 15- Multiphoton Lithography set-up (Made using 3ds MAX 2020)

Even though both set-ups utilize CAD for the fabrication of structures, different software are used at doing so. Galvo-scanner adopts a layer-by-layer approach. The desired pattern is loaded on the SAMlight software program, which slices it in parallel layers perpendicular to the structure's height. Another program controls the movement of the laser beam, in accordance with the directions that SAMlight provides. The structure is fabricated, one layer at a time. This set-up makes the design process fast and easy. Nano-cube offers a greater creative freedom, because structures are fabricated with the 3D design software, 3DPoli. Every structure is fabricated from scratch through commands in the 3DPoli environment. This can prove to be more time-consuming, but the user has a greater control over the fabricated structure.

The laser beam is expanded five times (5x) using a telescope to illuminate the full back aperture of the microscope objective lens and to achieve optimal focusing. Beam on/off is controlled by a mechanical shutter (Uniblitz) and laser power is adjusted with a motorized attenuator (Altechna). The fabrication process is monitored by a CCD camera mounted behind a dichroic mirror.

The sample to be polymerized is placed and stabilized on a holder. The holder can move in the xyz directions. The laser beam is focused on the sample with a focusing lens. A part of the beam is backscattered from the sample and collected with a CCD camera, which is connected to the computer. This apparatus is highly sensitive to alignment errors, so it is crucial that the sample, beam and lens are aligned correctly. The ideal scenario would be when the sample is perpendicular to the laser beam, as it is seen in Figure 16-a.

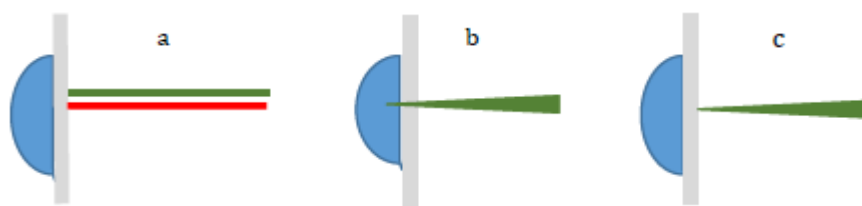


Figure 16- a) Ideal positioning of the sample, the incident (green) and the backscattered (red) beams. The interface is determined, b) Further into the material than it actually is, and c) Inside the glass.

When the sample alignment is finished, the laser needs to be focused at the interface between the glass substrate and the material. This is done by moving the sample closer to the focusing lens, while observing from the camera. When polymerization becomes visible, the laser is focused inside the material. Ideally, the laser is focused barely inside the material. That way, the base of the structure is fabricated at the interface and is attached on the glass substrate. If the interface is overestimated, the structure will not attach on the glass substrate and will be lost inside the material (Figure 16-b). On the other hand, if the interface is underestimated, part of the structure will be built inside the glass (Figure 16-c).

Once the interface is determined, the desired structure is loaded on the computer and the process is ready to start (Figure 17-a). It is common practice to begin fabricating the "tallest" parts of the structure first and moving closer to the interface as the procedure continues. The user needs to keep that in mind when working with nano-cube. In galvo-scanner however, the user needs only to input a dz step between layers (Figure 17-b). The last parts are fabricated at the interface that was determined (Figure 17-c). After the fabrication process is finished, the unpolymerized material is removed, leaving the polymerized structure on the glass.

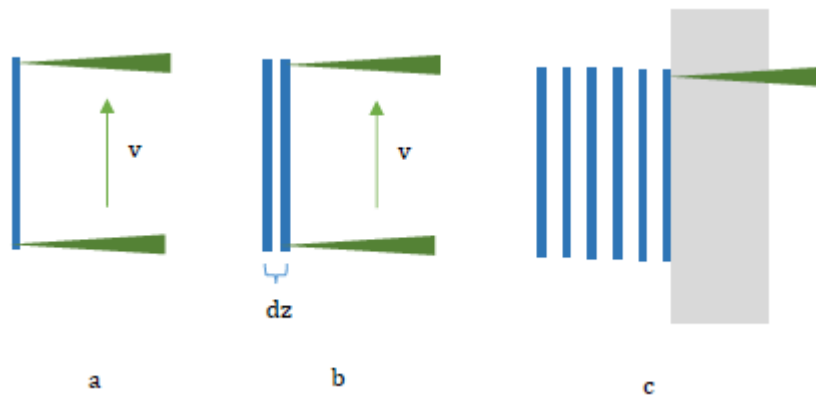


Figure 17- Fabrication of structure. a) Laser movement. Green is the incident beam and blue is polymerized material. b) Fabrication of consequential layers, and c) Last layer attaching on the glass substrate (grey).

nano-Dynamic Mechanical Analysis: The nanoscale mechanical measurements were achieved with Hysitron's *nano-DMA*, a dynamic testing technique equipped with CMX control algorithms that provide a continuous measurement of mechanical properties as a function of indentation depth. CMX stand for Continuous Measurement of X, where X can be hardness H, storage modulus E' , loss modulus E'' , complex modulus E^* and $\tan\delta$. The technique can be applied from ultra-soft hydrogels to hard coatings, with a greatly improved signal to noise ratio. Dynamic testing can be performed in a range of frequencies of 0.1-300Hz. A quasi-static force, up to 10mN, is applied to the indentation probe while superimposing a small oscillatory force of 5mN maximum. A lock-in amplifier measures phase and amplitudes changes in the resulting force-displacement signal. The dynamic response is modelled using two Kelvin-Voigt mechanical equivalents from which storage and loss modulus can be accurately determined. In Figure 18 $k_{s,i}$ are the elastic constants of the springs (N/m), $C_{s,i}$ are the damping coefficients of the dashpots (kg/s), ω is the applied frequency on the indenter and A_c is contact area of the tip and the material. All measurements were performed by Mr. Zacharias Vangelatos in UC, Berkley.

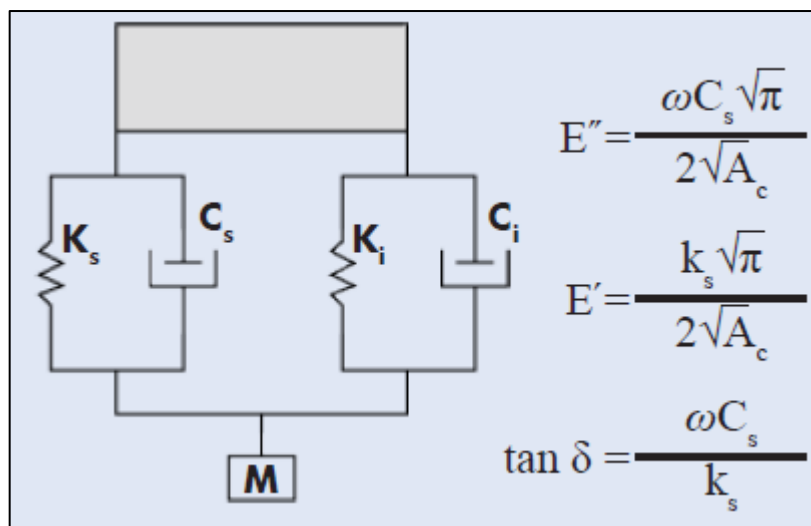


Figure 18- Schematic of the dynamic system and associated equations to measure viscoelastic properties.

CHAPTER 5: COMPUTATIONAL TOOLS

This chapter covers 3DPoli, Nano-cube's 3D design and fabrication software, and ANSYS Workbench Academic, which was used for the mechanical simulations of the various structures.

3DPoli: It has been previously mentioned that Nano-cube uses a software named 3DPoli to fabricate microstructures. Additionally, the software is also used for the design of microstructures by introducing variables and writing commands. Through the software the user can control the values of defined variables, the shutter, attenuator position, the movement of the stages and the velocity which they move. Moreover, the user can control the piezoelectric stages (XYZ) and the mechanical stages (IJK) individually. The code can be compiled any time to view what has been designed, which favours a trial-and-error approach while creating microstructures. All the commands are shown in the following table.

Table 3

Command	Translation
Dvar(\$x)	Define variable "x"
Var(\$x,0)	Value of variable "x" is equal to 0
SetVel(XYZ,100)	Define the velocity of XYZ stages as 100.
SetHome(XYZ)	Define current spot as 'home' for stages XYZ
MoveA(XYZ,0,0,0) / LineA(XYZ,0,0,0)	Move XYZ absolutely to point (0,0,0)
MoveR(XYZ,0,0,0) / LineR(XYZ,0,0,0)	Move XYZ relatively by (0,0,0)
Shutter(0) / Shutter(1)	Close shutter / open shutter
For(\$x,0,10,1) end	Repeat whatever is between 'for' and 'end'. Start counting from 0 until 10, with a step of 1.
Procedure(A) end	Name a series of commands 'A'.
RunProc(A)	Run the procedure named 'A'.

For simplicity's sake, the XYZ stage was used above, but the IJK stage can be used in any of the commands as well. The XYZ stage have more accurate movement but are limited to move from 0-100 μ m. The IJK on the other hand, move from 0-5000 μ m and are generally used for larger actuations. 'Move' and 'Line' commands are basically identical. However, they can be used appropriately to distinguish between movements with the shutter open (Line) or close (Move). The design process can be scaled down to individual lines which make up the entire structure. Unfortunately, there is no command for creating circles, but there are alternatives routes by using trigonometric functions. The hybrid material used may not interact with the laser beam apart from multiphoton absorption, but polymerized material is a scatter hazard for the laser pulses. It is common practice to begin fabricating the 'highest' parts of each structure and gradually moving closer to the glass substrate, so the laser beam does not interact with any polymerized material. Galvo-scanner does this automatically, but in Nano-cube the user must create each structure with that in mind. The 3DPoli interface is shown in Figure 19.

Using 3DPoli various microstructures (meta-atoms to be exact) were created. With the 'For' command they can be expanded in all three directions, making possible the creation of a 3D lattice in a simple and fast manner. On top of that, with the 'Procedure' command, the whole 3D lattice can be called directly for fabrication. All 3D lattices were fabricated by following this methodology.

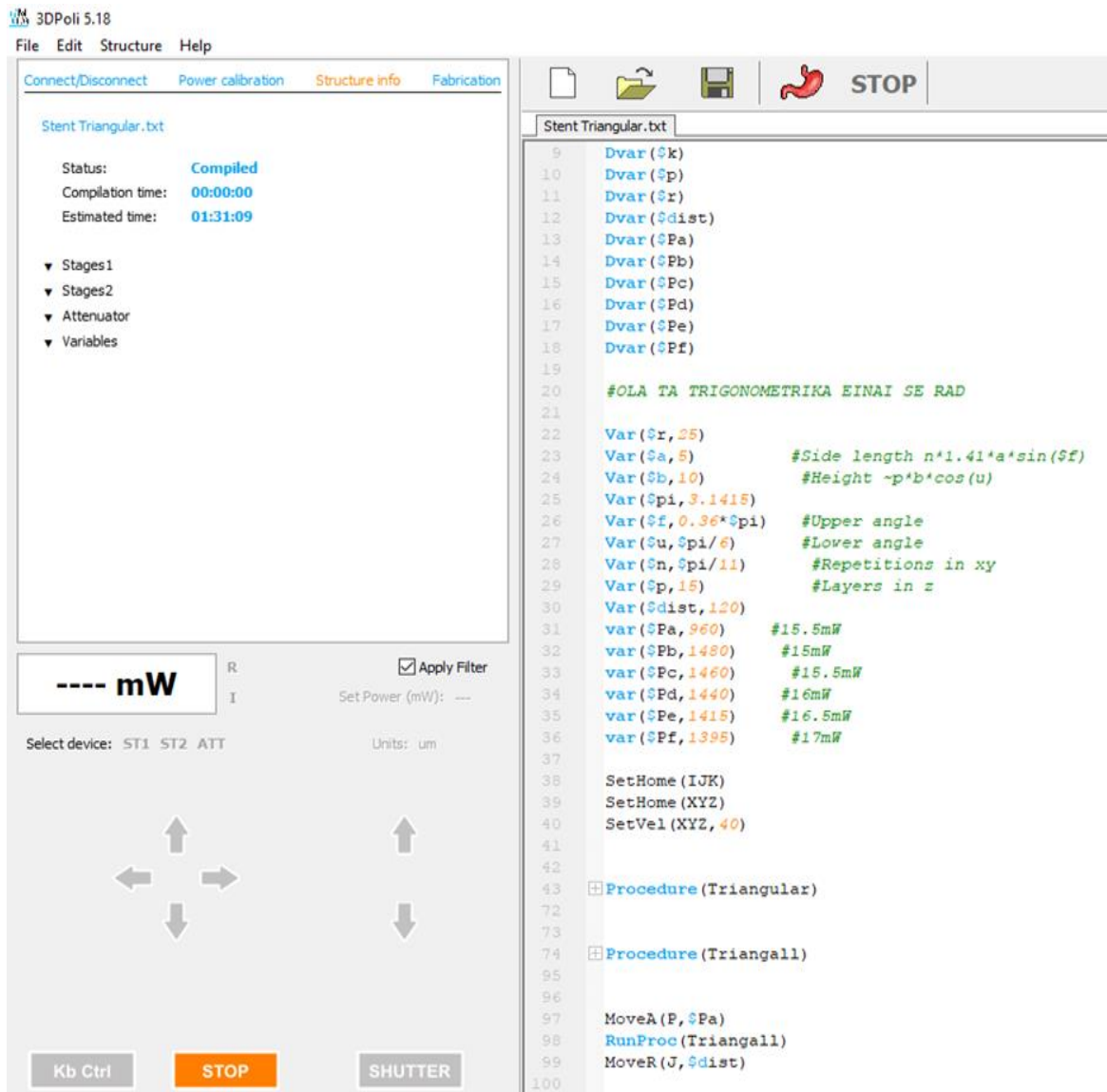


Figure 19- The interface of 3DPoli. The loaded structure is the auxetic stent.

ANSYS Workbench Academic: Before proceeding in the fabrication of a microstructure, a mechanical simulation of the pattern was conducted first with the engineering simulation and 3D design software, ANSYS. ANSYS offers various options for realistic simulations, one of which is mechanical. The simulation is based on the Finite Element Method (FEM), which divides the geometry in independent elements (meshing). Smaller elements result in a finer and more detailed mesh which makes the simulations more accurate. The structure is designed in the software's environment by connecting shapes and solids instead of writing a code. There is the option of choosing an already existing material for the structure or creating a new one. The user can choose the type, magnitude and position of the mechanical loads exerted on the structure and which results should be simulated (Stress, strain etc..). After the program has finished the simulation, the user can view and save the results. In Figure 20, 3D triangular structures are shown. The bottom of the geometry is defined as immovable, while a downwards forces is applied on its top.

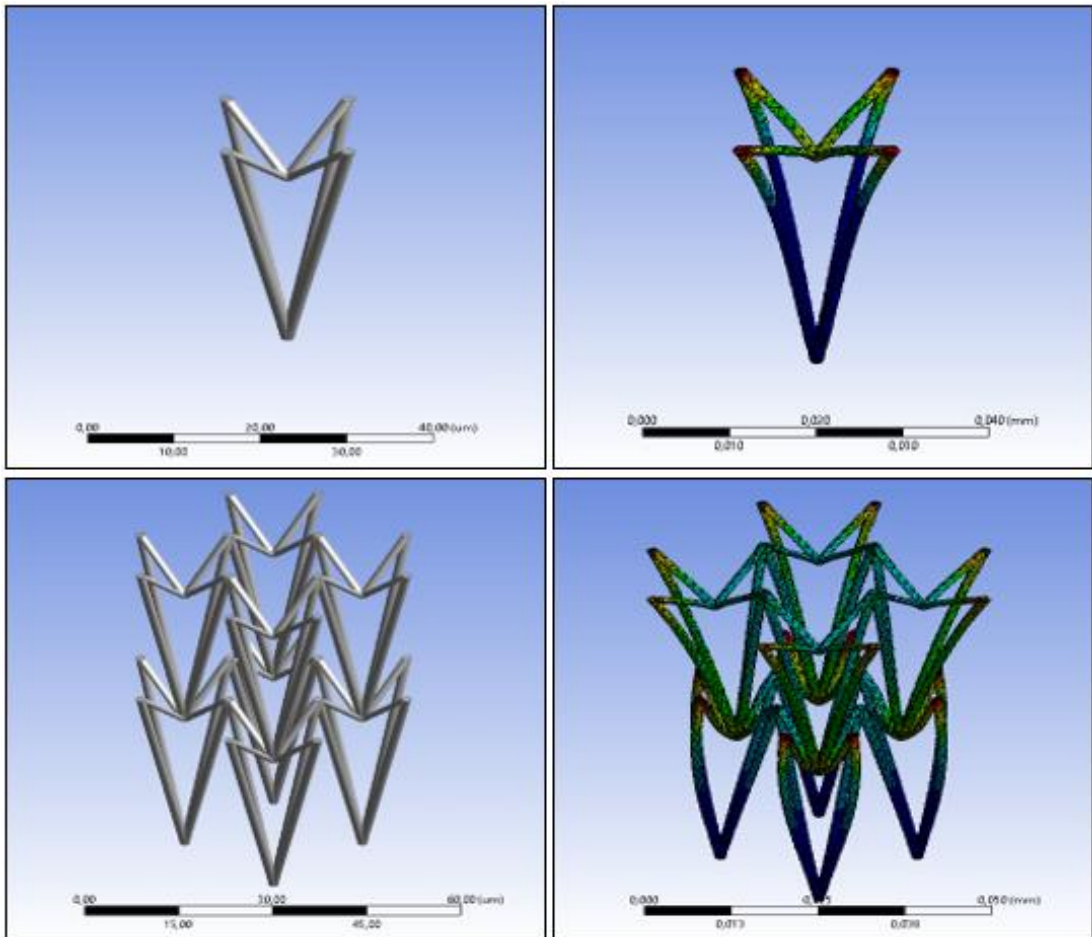


Figure 20- Simulations sample of the ANSYS Workbench Academic.

CHAPTER 6: RESULTS and DISCUSSION

Mechanical Characterization

The synthesis of the hybrid material used in *MPL* is extensively presented in Chapter 4. However, little to no information about its mechanical properties are available. There have been various attempts to characterize the bulk properties of commercially available materials used in *MPL*, but none of them provide with a reliable and accurate result [83–85]. They fail to consider the viscous nature of the polymer materials i.e. the time-dependence of stress and strain. Moreover, characterizing the mechanical properties of structures made through *MPL* is challenging due to their μm size. To counter this setback a different approach was adopted, using films of polymerized material and conventional indentation methods [86]. The characterization that concluded from this approach cannot be accurately applied in *MPL* because the mechanical properties of the hybrid material are polymerization-dependent, and by extension method-dependent. So, in order to properly characterize the hybrid material for use in *MPL*, static and dynamic tests need to be performed on samples fabricated with *MPL*.

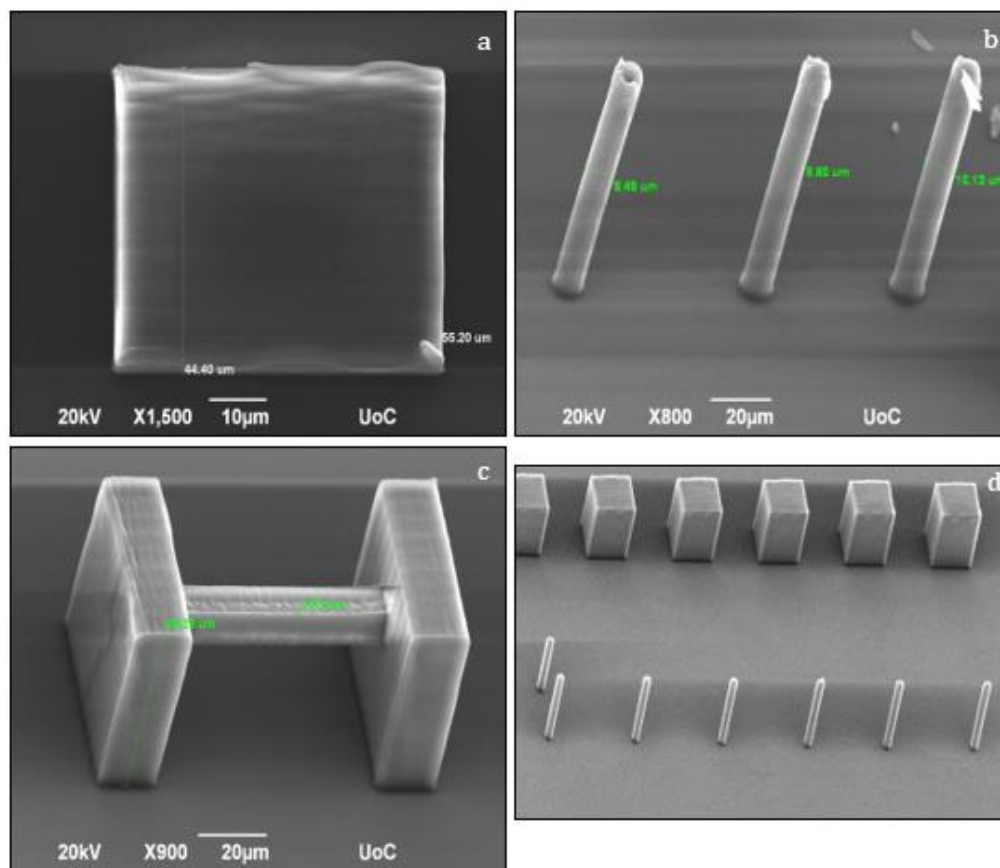


Figure 21-SEM images of a) Cubes, b) Upright cylinders, c) Vertical bars, and d) Arrays on substrate.

Three different geometries were considered for the characterization: cubes, upright cylinders and vertical bars (Figure 21). The structures were fabricated in the Galvo-scanner set up and the fabrication conditions were the same for all three geometries. The energy ranged from 24mW to 40mW with a 2mW step, for a total of 9 energy values. Fabrication speed was constant at 10 $\mu\text{m/s}$ for all structures. 8 copies were fabricated for each energy value, for a total of 72 structures for each geometry. The cubes were used in *nano-DMA* tests to measure storage modulus, loss modulus and hardness (Figure 22), while the upright cylinders were used in in-situ SEM experiments to measure Poisson's ratio (Figure 23). The vertical bars would have been used in

nano-DMA tests in case the cubes did not provide with reliable results. The frequency ω in the *nano-DMA* tests was 220Hz for all measurements.

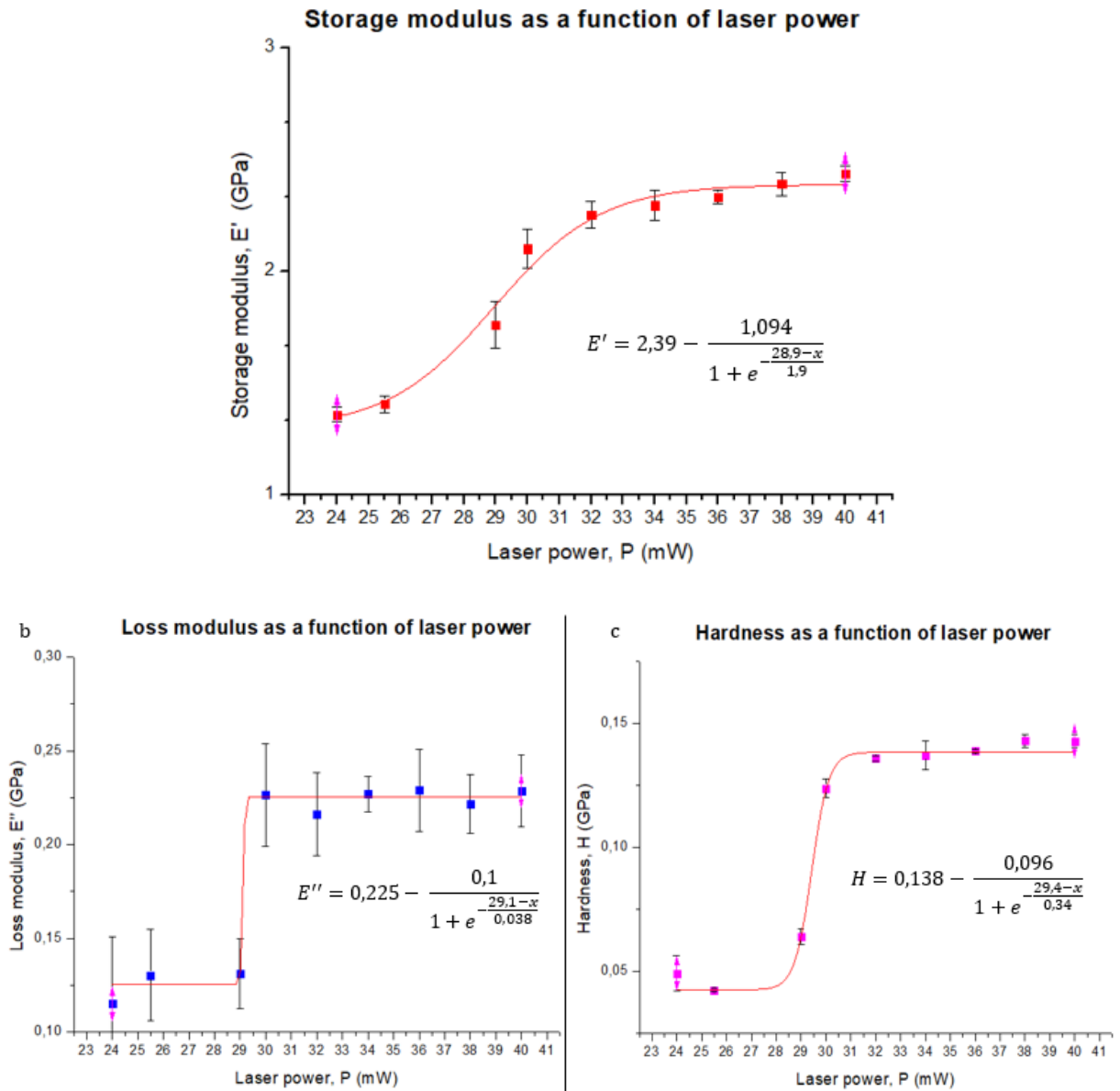


Figure 22- Storage modulus, loss modulus and hardness as a function of laser power.

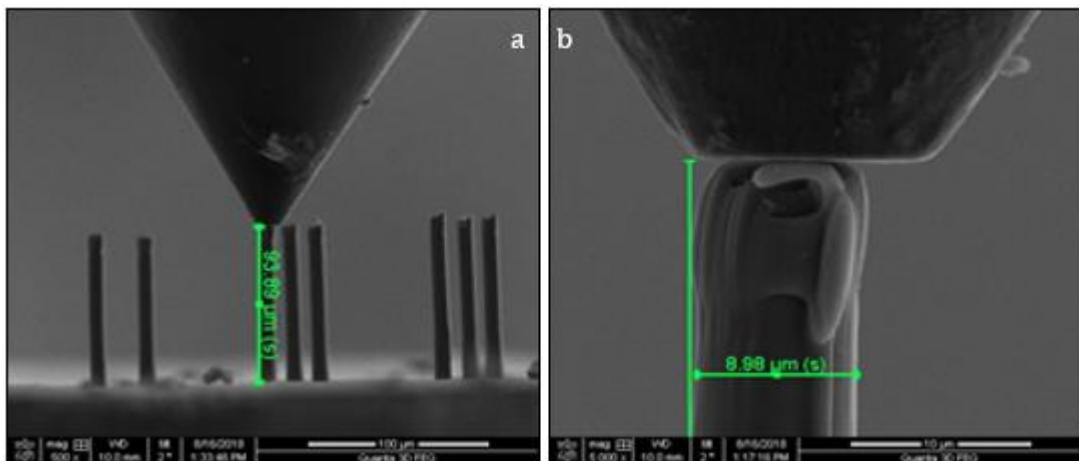


Figure 23- In-situ SEM images of the cylinders.

It is evident at a first glimpse of the data, that the mechanical properties of the material do not follow a linear trend as the laser power increases. A Boltzmann curve fits the data far more accurately. Moreover, the Loss modulus and Hardness curves appear to have a step-function behaviour in which the y-axis jumps abruptly to a higher a value, in the area of 29-30mW. In Figure 22-b, Loss modulus is around 0.125GPa for low laser powers and 0.225GPa after the jump. Loss modulus has the most abrupt jump among all three curves. In Figure 22-c, Hardness is roughly 0.04GPa for low laser powers and 0.138GPa after the jump. However, it appears to slightly increase as the laser power keeps increasing. In Figure 22-a, Storage modulus appears to combine a linearly increasing trend throughout the graph with the a less-abrupt jump in the 29-30mW region.

The step behaviour at 29-30mW appearing in all graphs to a degree, could be attributed to the polymerization threshold. During fabrication, polymerization naturally spreads outside of the voxel, with crosslinking occurring between the different molecules. As the laser beam 'writes' the structure inside the material, different voxels combine and form a solid. There is a certain amount of bonds each molecule can create and so this crosslinking cannot continue indefinitely. In other words, there is a saturation on 'how much' the material can be polymerized. At lower laser powers, this limit has not been reached yet. However, as laser power increases the material reaches this threshold and is almost polymerized in its entirety. This saturation most likely occurs in the region of 29-30mW where the mechanical properties of the material switch to a higher value. The validity of this assumption could be tested by irradiating the cubes with a UV lamp after development.

In contrast with the above, Poisson's ratio was found to be independent of laser power with a constant value at 0.490 ± 0.002 . The original dimensions of the cylinders before the measurements are shown in Figure 23. The indenter compresses the cylinder whose height and diameter are measured with a high-accuracy camera. Poisson's ratio is calculated from its original definition in Chapter 1.

Metastructures

As an introduction to *mechanical metamaterials*, relatively simple geometries were considered for fabrication. All structures were fabricated with the Nano-cube setup due to its superior resolution. A rhombic or octahedron-like geometry is shown in Figure 24. Octahedra structures are excellent strong-lightweight materials and their properties have been studied in different structural arrangements. The geometric parameters of the unit cell's rods (length, width, angles) affect the outcoming properties of the *metamaterial*. This can be taken one step further with structural hierarchy, where features across three length scales have been achieved, greatly improving the mechanical properties [87].

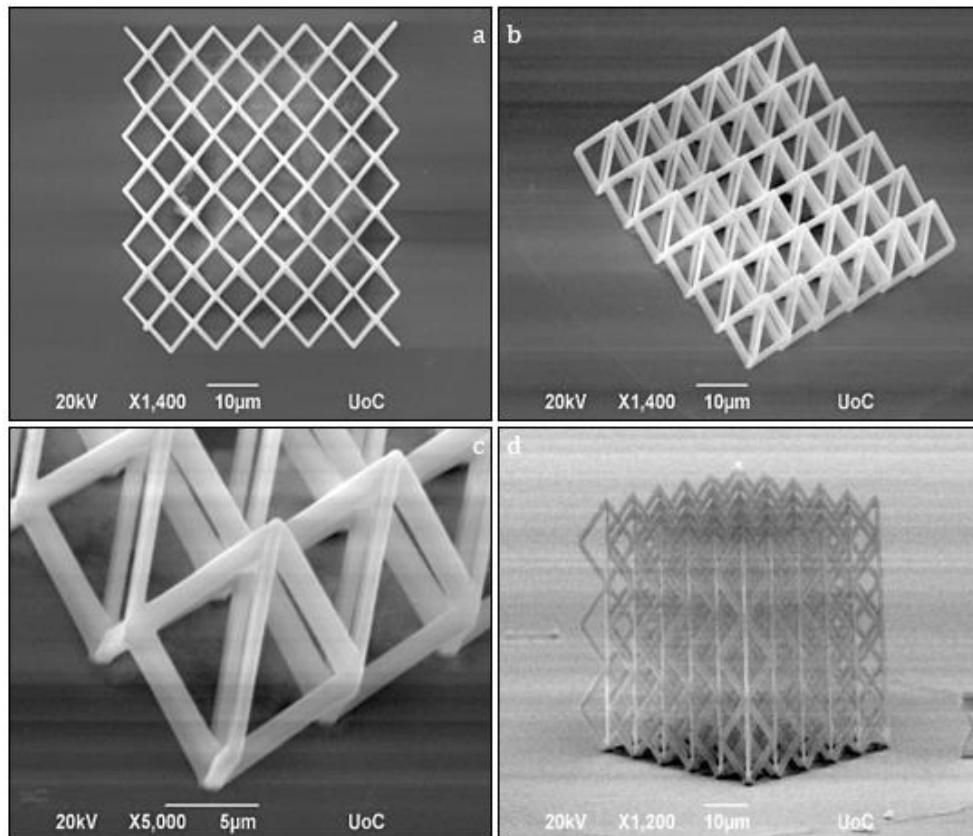


Figure 24- SEM images of rhombic structures fabricated in the Nano-Cube with $100\mu\text{m/s}$ and 11mW , a) Top view, b) Perspective view, c) Close-up of the unit cell, and d) Side view of 3D lattice.

Figure 25 shows a lattice based of the so-called 'bowtie' structure, which in essence is a re-entrant hexagon. 'Bowtie' is a well-researched structure, known for its *auxetic* properties, studied with different methods in various length scales across the literature [88]. The *auxetic* behaviour depends on the number, length and thickness of its rods as well as the angles between them. The unit cell of Figure 25 in particular, is $10\mu\text{m}$ in all directions and consists of 4 'bowties' angled at 45° between them. The unit cell can be expanded to create 2D and 3D lattices.

Another re-entrant type structure is shown in Figure 26. The re-entrant triangular is an *auxetic* material, whose *auxetic* behaviour is known to depend on the length of its ribs and the angle which is formed between them [89,90]. The unit cell in Figure 26 is only a few μm in size, consisting of 4 rods at a 90° angle, and, in the same manner as the 'bowtie', it can be used as the building block for a 3D microlattice. Also, a unit cell with 2 rods was considered creating a 2D re-entrant triangular. Figure 27 shows parallel sheets of this structure connected with rods in between. This arrangement exhibits *auxetic* properties as well.

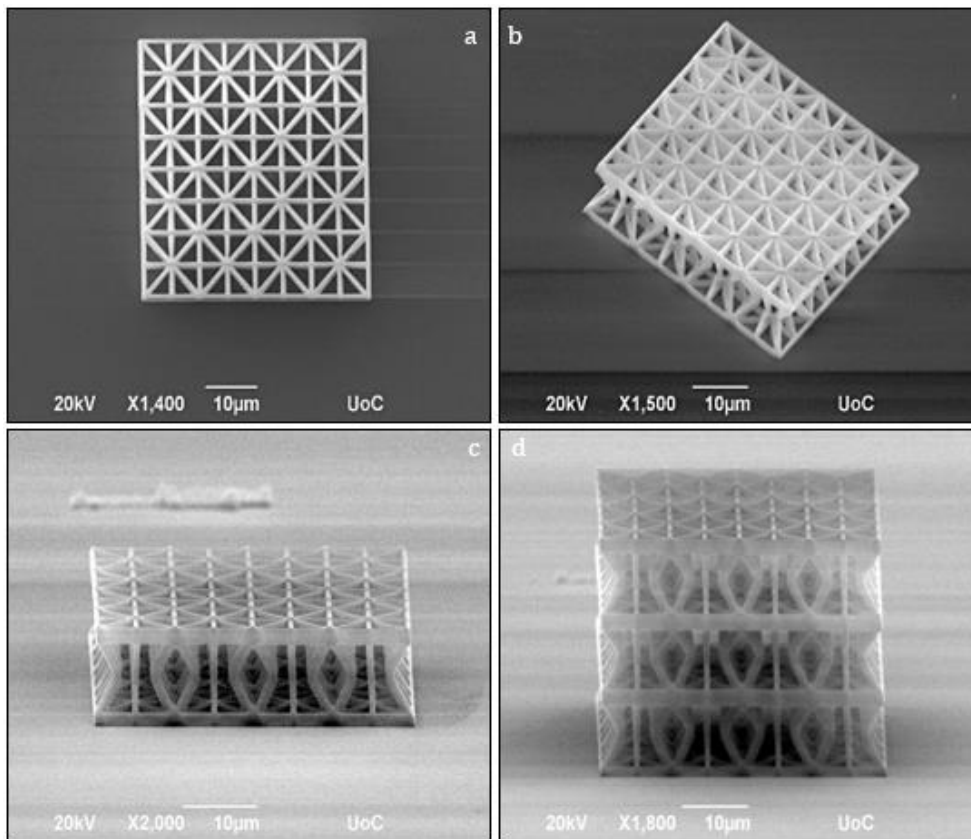


Figure 25- SEM images of 'bowtie' structures fabricated in the Nano-Cube with $100\mu\text{m/s}$ and 11mW , a) Top view, b) Perspective view, c) Side view of 2D lattice, and d) Side view of 3D lattice.

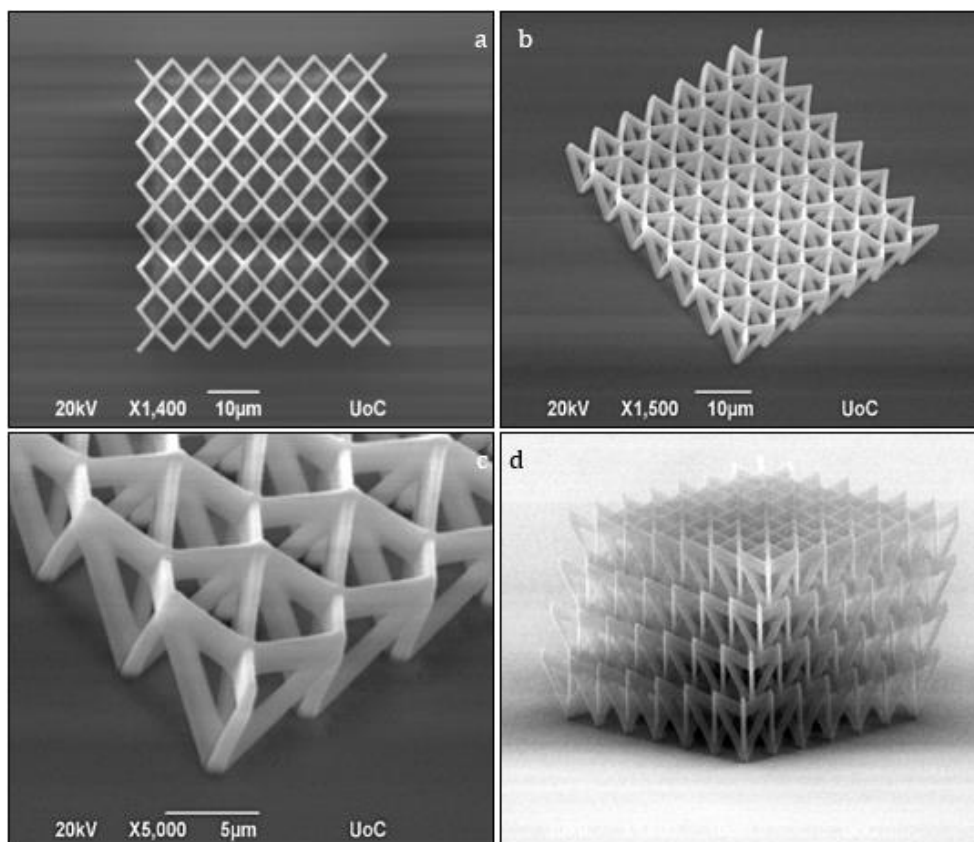


Figure 26- SEM images of the 3D re-entrant triangular structures fabricated in the Nano-Cube with $100\mu\text{m/s}$ and 11mW , a) Top view, b) Perspective view, c) Close-up of the unit cell, and d) Side view of 3D lattice.

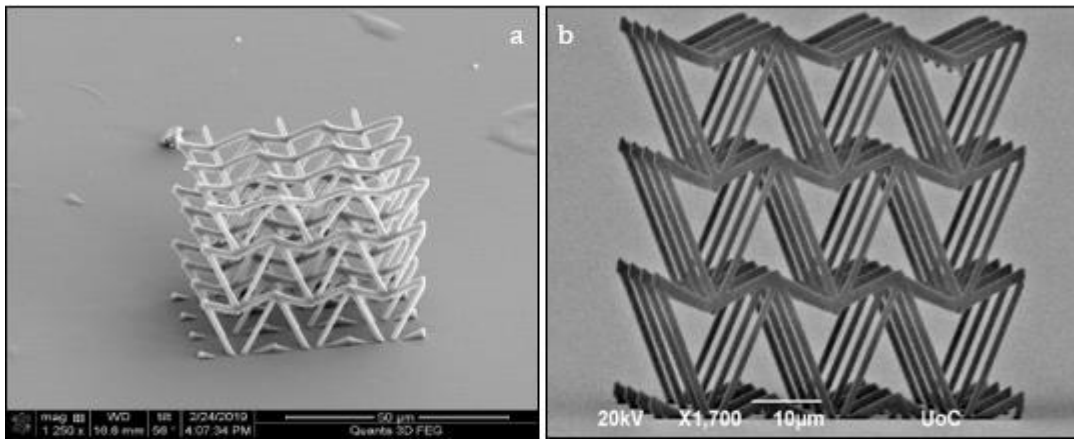


Figure 27- SEM images of the 2D re-entrant triangular structures fabricated in the Nano-Cube with $100\mu\text{m/s}$ and 11mW , a) Perspective view, and b) Side view.

In the next step, more elaborate structures were investigated. In Figure 28 and Figure 29 octahedron-based lattices are shown. The unit cell consists of 3 octahedra rotated about its center to create a truss-like structure. The arrangement of the octahedra inside the unit cell is not the same. In Figure 28, the top of each octahedron is rotated 45° along the x (or y) axis. In Figure 29, each octahedron is aligned with each primary axis. The resulting 3D lattice is highly durable, lightweight but strong and can regain its original shape even after large strains are applied.

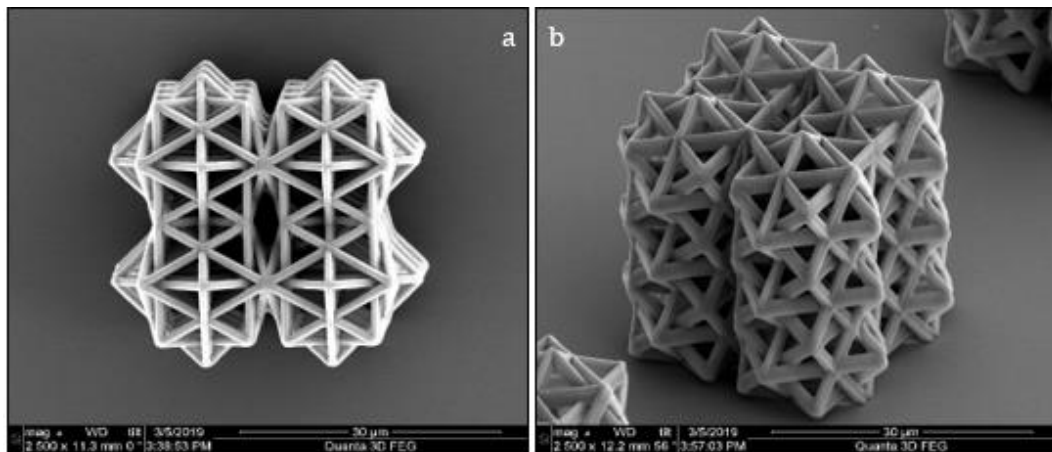


Figure 28- SEM images of the first arrangement of octahedra fabricated in the Nano-Cube with $100\mu\text{m/s}$ and 11mW , a) Top view, and b) Perspective view.

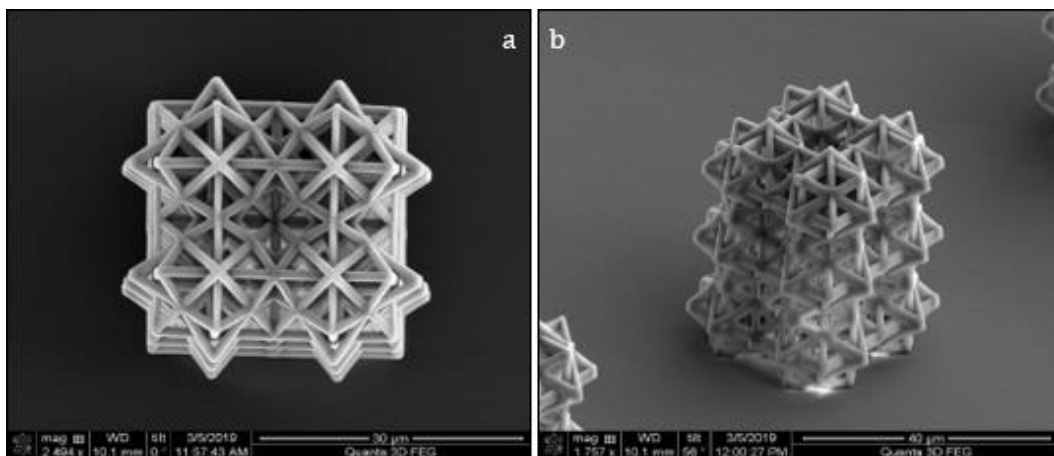


Figure 29- SEM images of the second arrangement of octahedra fabricated in the Nano-Cube with $100\mu\text{m/s}$ and 11mW , a) Top view, and b) Perspective view.

A unique arrangement for tensile measurements of metastructures, inspired from the work of J. Bauer et. al [91], is shown in Figure 30. The structure under study is fabricated between two frames. When the top frame is pushed down, the in-between structure is elongated. In our case, a spring-like structure, resembling the shape of a car jack, is inside the frames.

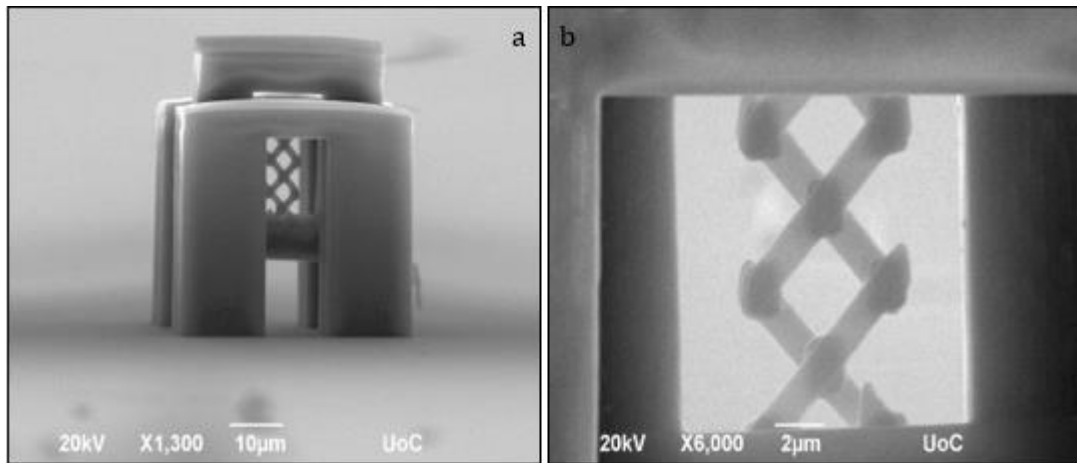


Figure 30- SEM images of the tensile test structure fabricated in the Nano-Cube with $100\mu\text{m/s}$ and 9mW , a) Side view, and b) Close view.

A *metamaterial* that twists when pushed is seen in Figure 31. The structure was inspired from the wrapping of caramels that has a similar response when pushed. The ‘spinner’ unit cell consists of 3 rods that spiral around the center as the height changes to a total of 180° turn. The plate in the middle will rotate as the structure is pushed downwards.

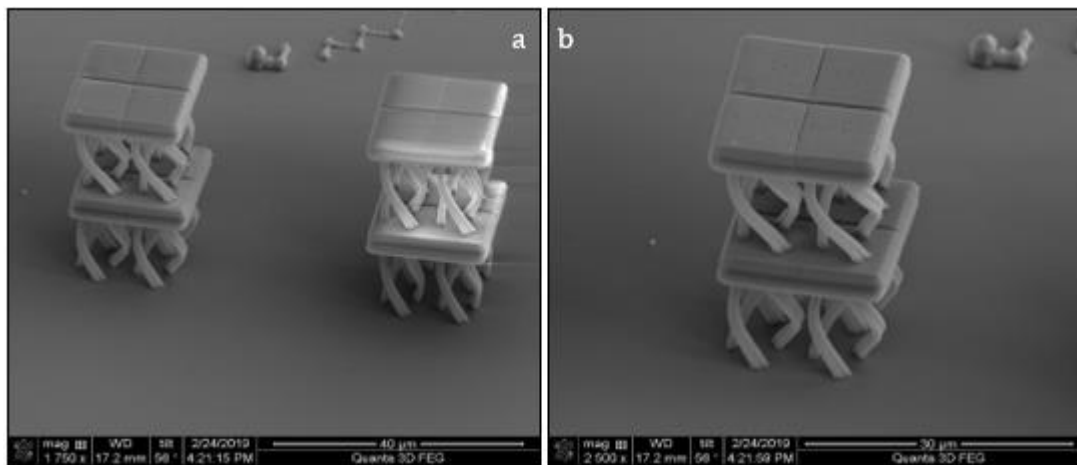


Figure 31- SEM images of the ‘spinner’ structure fabricated in the Nano-Cube with $100\mu\text{m/s}$ and 10mW , a) Perspective view, and b) Close view.

Finally, the 2D re-entrant triangular was used as the unit cell to fabricate a cylindrical stent (Figure 32). The stent has a diameter of $50\mu\text{m}$, and its height can be easily altered by changing the number of layers. The stent was originally made as tall as 90nm , but due to limitations of the *nano-DMA* had to be reduced to 60nm .

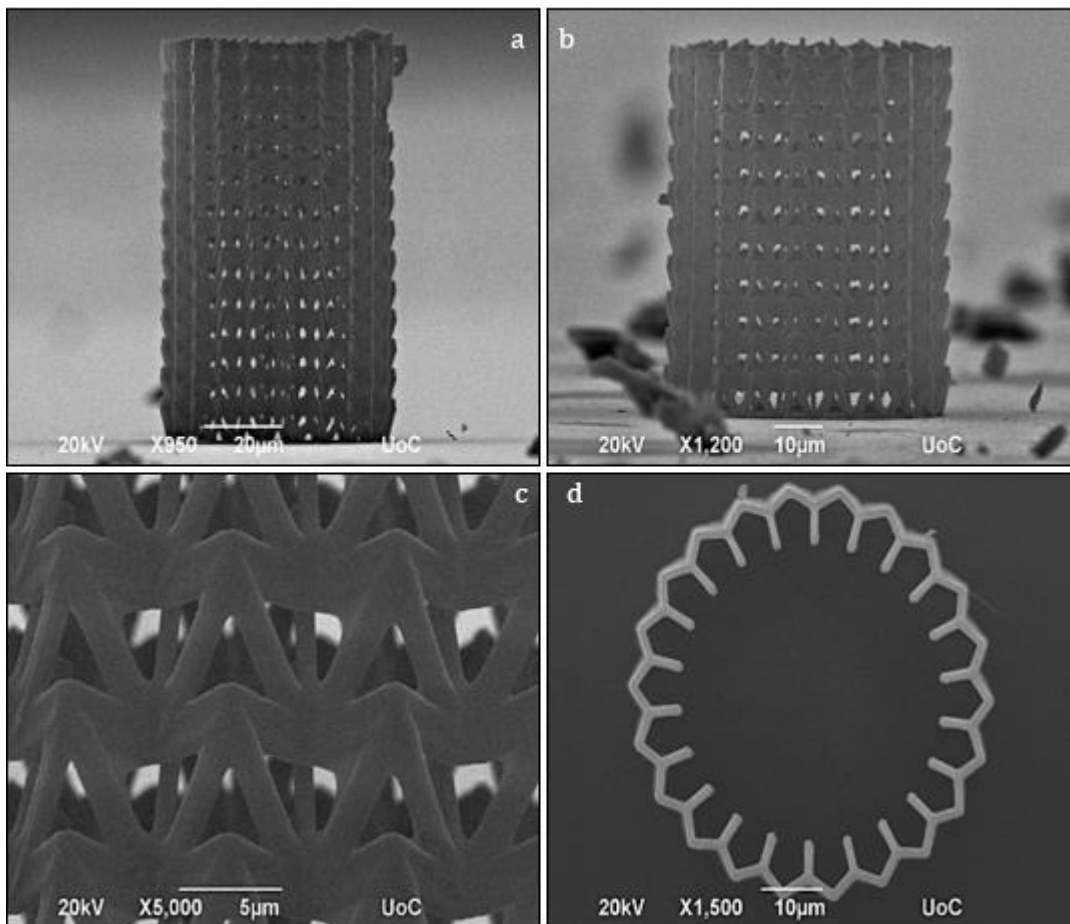


Figure 32- SEM images of the 2D re-entrant triangular stent fabricated in the Nano-Cube with 100µm/s and 10mW, a) Side view with ~60nm height, b) Side view with ~40nm height, c) Close view of the cylindrical lattice, and d) Top view.

The rhombic, bowtie and triangular structures were fairly simple to design, with the most demanding aspect being diagonal movements with the XYZ stages. These were achieved by using all three axes of the LineR(XYZ...) command. The octahedra structures required each octahedron to be rotated at different angles. On the second arrangement this is not a hard thing to do, as simple diagonal movements sufficed, even though the image of three co-centered octahedra could get quite confusing. The first arrangement though was not as simple, because the octahedra did not coincide with the primary axes. Their design was achieved by inserting trigonometrical functions inside the 'Line' commands. The tensile test structure was not difficult itself. The framing however, had to be redone numerous times so it would not bend during measurements. In the spinner structure, circular movements were achieved quite simple, just by using trigonometrical functions so the points would fall on a circle. On the other hand, the stent structure did not require just a circular framework, but also individual elements to rotate around their axes. This was achieved by using two 'For' commands, one inside the other, one for moving the center of each triangular along the circle and the other rotating each triangular appropriately so they would face the center of the stent. The code contained defined variables instead of numbers. Even though this made it harder to write, the microstructures' size and arrangement could be changed faster by simply changing the values of said variables.

Mechanical Measurements

The 2D-triangular, spinner and *auxetic* stent structures were measured in the *nano-DMA*. The maximum force on the 2d-triangular exceeded $200\mu\text{N}$ and maximum strain was approximately 40%, with the middle layer absorbing most of the deformation (Figure 33). Despite the strain exerted on it being quite large, the structure appears to return to its original size with no signs of failure. The spinner structure was not as stable during measurements and moved sideways when compressed (Figure 34). Furthermore, the structure absorbs the force applied from the indenter tip by moving its rods outwards, instead of spinning, which reduces its total rotation. Despite this, minor rotation of the middle plate can be observed, but the structure's design needs refinement in order to address the aforementioned issues. The stent structure was quite sturdy, withstanding more than 1mN of displacement force (Figure 35). However, its deformation is not uniform, with some parts moving inwards and other slightly protruding. This can be attributed to its ends not being able to move freely, with its base stuck with the glass substrate and its top in contact with the indenter tip. Quite surprisingly, the stent appears to return to its original size with minor alterations, despite withstanding considerable axial deformations. The real-time response of the structures can be seen in the videos at Mendeley data, <http://dx.doi.org/10.17632/6sb5bhzc3.1>.

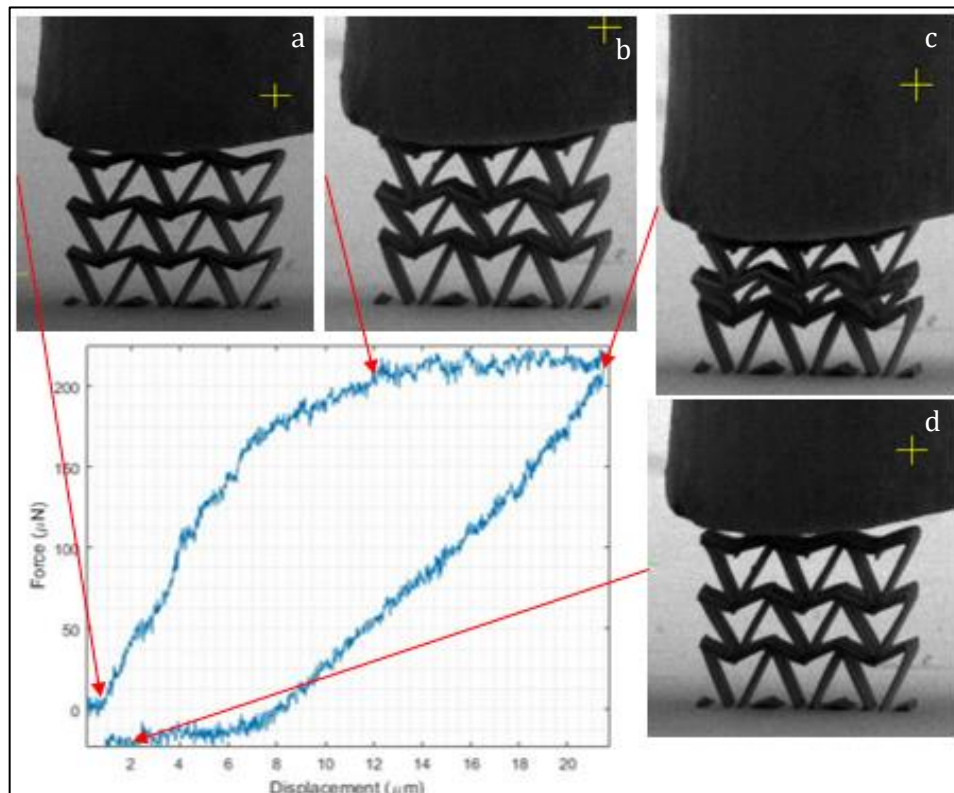


Figure 33- Mechanical measurements and SEM images of 2D-triangular [UC,Berkeley]. a) Beginning of the test at 0% strain, b) $200\mu\text{N}$ of force and 24% strain, c) 42% strain, and d) End of test.

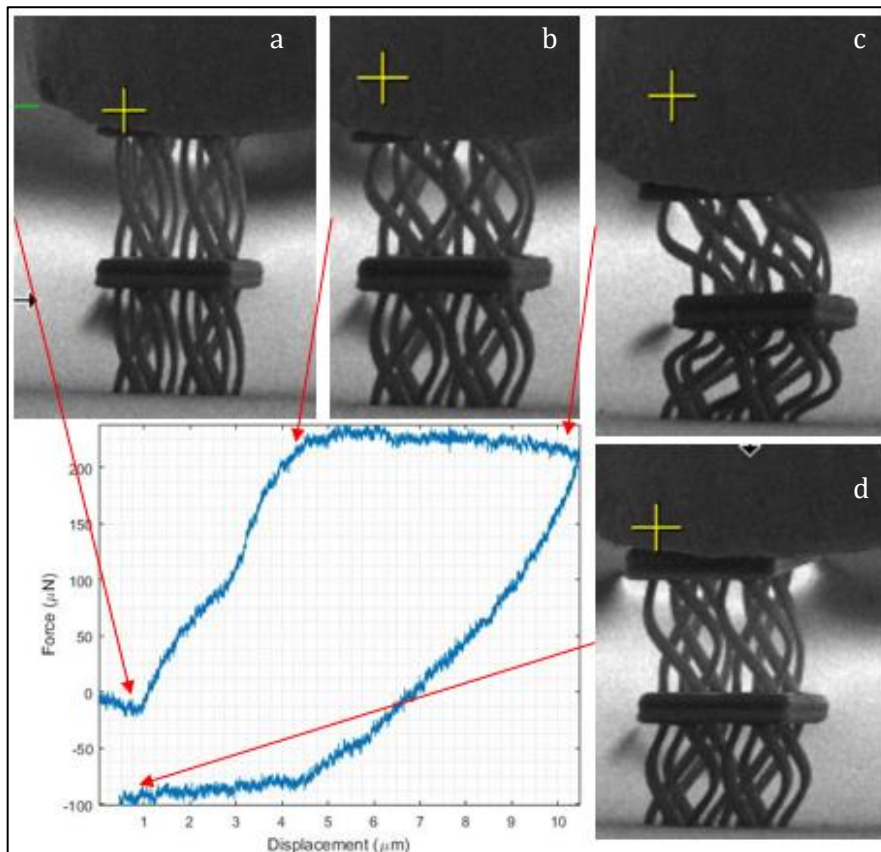


Figure 34- Mechanical measurements and SEM images of spinner [UC,Berkeley]. a) Beginning of test at 0% strain, b) 220 μ N of force and 10% strain, c) 25% strain, and d) End of test.

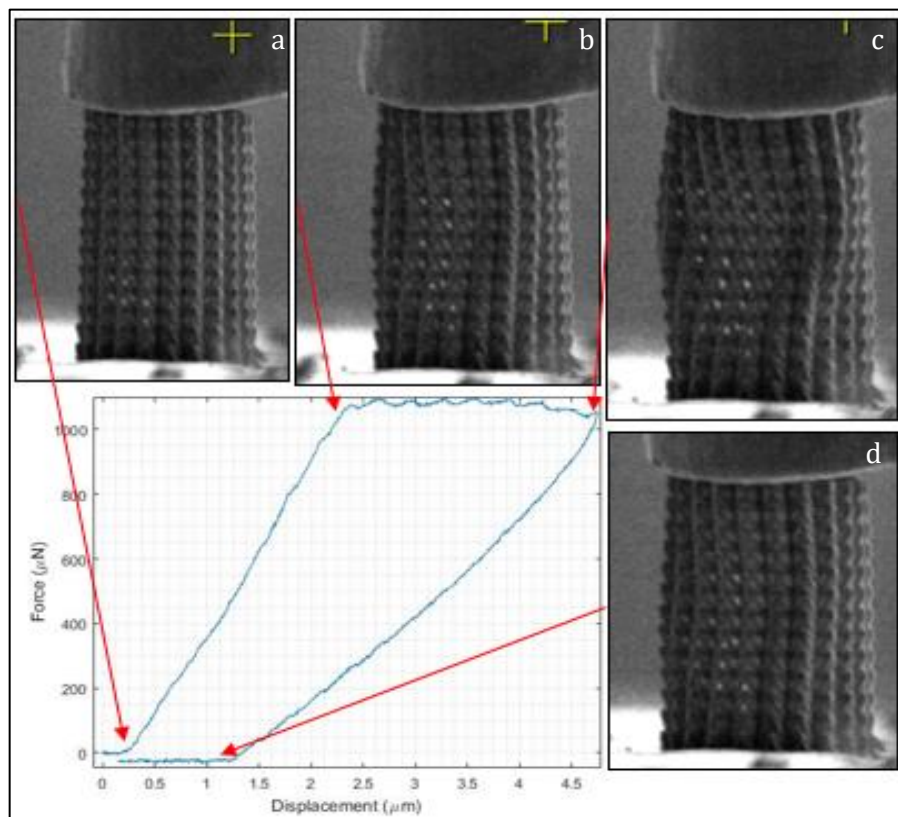


Figure 35- Mechanical measurements and SEM images of auxetic stent [UC,Berkeley]. a) Beginning of the test at 0% strain, b) 1.05mN of force and 2% strain, c) 5.2% strain, and d) End of test.

CONCLUSIONS and FUTURE PROSPECTS

Complex 3D *mechanical metamaterials* were successfully fabricated and had their mechanical response measured. *MPL* proved to be a prime candidate for realizing 3D *mechanical metamaterials* in the μm scale, offering superior resolution and excellent result repeatability as a one-step fabrication process. Arguably, the biggest drawback of *MPL* is its limitation of using exclusively polymer materials. However, this is a minor issue when considering *metamaterials*, because their geometry is of foremost importance, affecting mechanical properties the most. The mechanical properties of the hybrid material used in *MPL* were measured and later used in the mechanical simulations in ANSYS Academic. Every geometry could be reliably investigated before proceeding to fabrication. *Nano-DMA* performed the mechanical characterization of microstructures, which could be observed and recorded real-time. This close-up view of the microstructures provided us with important insight on how the *metamaterials* will perform in potential applications. In general, the *metamaterials* tested were highly flexible and elastic, with no signs of mechanical failure after been deformed. The work presented here could pave the path for integrated *metamaterial* devices

The hybrid material used in *MPL* demonstrates a switching behaviour in its mechanical properties, most prominent of which is Hardness, displaying a three-fold increase over a span of a few mW of laser powers. In comparison, Poisson's ratio was found to be constant at 0.490 ± 0.003 , a common value for polymers. As of now, it is yet uncertain where the switching behaviour is attributed to. Most likely it is due to the polymerization threshold of the material not having been reached in lower laser powers. In order to confirm this, the cubes used in the characterization could be illuminated with UV light after development and then repeat the *nano-DMA* measurements. If the previous assumptions are correct, the properties of all cubes should be that of the higher laser powers, regardless of the laser power used to fabricate them. On a different note, the characterization experiments could be repeated with a larger range of laser powers. This would reveal the whole spectrum of available mechanical properties of our material. Nevertheless, the switching behaviour could be exploited to fabricate microstructures that have varying mechanical properties. For example, intervertebral disc spacers are implants with variable hardness. They are used to replace degenerated spinal discs that have similar mechanical properties. Furthermore, a hard material tends to scratch a softer material when in contact. Varying the hardness of a structure could potentially reduce the hardness-mismatch at the contact area and therefore reduce the wearing of the materials. Another application includes cantilevers that have a different resonant frequency due to the variation of their stiffness, functioning as physical, biological or chemical sensors. Despite any potential applications, it should not be taken for granted that the mechanical properties of a polymer material do not decay over time. Before moving on to *mechanical metamaterial* devices, the stability of the material's mechanical properties should be investigated.

The 'spinner' structure did not work as intended, as it was not stable under compression. The architecture could be refined by adding a connection at the middle of the three rods to hold them together. Alternatively, a simpler design could be adopted where rotation is achieved by the diagonal lines of a cube or rectangular. Despite this, it provided with useful insight on metastructures that rotate when pushed. This rotation behaviour is the mechanical equivalent to optical activity, where a geometry rotates when light incidents on it. Such *metamaterials* could be utilized in mechanical waveguide devices, to guide mechanical waves in preferential directions. Specifically, they could be used in devices for mode conversion, traversing from axial forces to rotational movements and vice versa.

There are various geometries that result in the counter-intuitive property of Poisson's ratio. The 3D-triangular was chosen because it is a relatively simple geometry that had not been extensively

studied compared to other *auxetic metamaterials*, such as the bowtie. The 2D-triangular lattice displayed a strong elastic behaviour, enduring strains up to 40% and returning to its original shape. Such arrangements could be used as tunable microfilters, whose pores close/open homogeneously in all directions as stress is applied. This isotropic expansion/compression could also be used in cardiac patches. The heart expands and compresses simultaneously in all directions. Standard cardiac patches cannot keep up with this motion because as they compress in one direction they expand in the other. Negative Poisson's ratio could be utilized in *auxetic* patches which will not have this disadvantage.

The *auxetic* stent based on the triangular could withstand a considerable bending force of more than 1mN. Even though it was not strained as much as the 2D-lattice due to its small height and restricted ends, it was steeply curved in specific areas but showed no signs of failure post-bending. *Auxetic* stents push back laterally as blood stretches them axially, so the negative Poisson's ratio is a preferential property. As of now, *auxetic* stents are commercially available, mostly for esophageal or arteriac use. However, for smaller veins they have yet to be employed. The *auxetic* stent of our work was 50 μ m in diameter, making it suitable for eye operations and glaucoma treatment. There is still much work to be done before it becomes available for surgeries. Firstly, its suitability in the eye environment needs to be confirmed. It is a known fact that DMAEMA is a biocompatible material. Nevertheless, cell cultures should be grown on the *auxetic* stent. Secondly, the structure does not demonstrate a pure *auxetic* behaviour when compressed in the *nano-DMA*, bending in certain areas instead of a uniform response. This is a combination of its ends being restricted and it being too short. A uniform response could be observed if the stent was made longer and measured again with the *nano-DMA*.

REFERENCES

- [1] Pendry J B, Holden A J, Robbins D J and Stewart W J 1999 Magnetism from conductors and enhanced nonlinear phenomena *IEEE Trans. Microw. Theory Tech.*
- [2] Bückmann T, Thiel M, Kadic M, Schittny R and Wegener M 2014 An elasto-mechanical unfeelability cloak made of pentamode metamaterials *Nat. Commun.*
- [3] Kadic M, Bückmann T, Stenger N, Thiel M and Wegener M 2012 On the practicability of pentamode mechanical metamaterials *Appl. Phys. Lett.*
- [4] Christensen J, Kadic M, Kraft O and Wegener M 2015 Vibrant times for mechanical metamaterials *MRS Commun.*
- [5] Gatt R and Grima J N 2008 Negative compressibility *Phys. Status Solidi - Rapid Res. Lett.*
- [6] Baughman R H, Stafström S, Cui C and Dantas S O 1998 Materials with negative compressibilities in one or more dimensions *Science (80-.)*.
- [7] Nicolaou Z G and Motter A E 2012 Mechanical metamaterials with negative compressibility transitions *Nat. Mater.*
- [8] Lakes R and Wojciechowski K W 2008 Negative compressibility, negative Poisson's ratio, and stability *Physica Status Solidi (B) Basic Research*
- [9] Prall D and Lakes R S 1997 Properties of a chiral honeycomb with a poisson's ratio of — 1 *Int. J. Mech. Sci.*
- [10] Milton G W 1992 Composite materials with poisson's ratios close to - 1 *J. Mech. Phys. Solids*
- [11] Lakes R 1987 Foam structures with a negative poisson's ratio *Science (80-.)*.
- [12] Kolken H M A and Zadpoor A A 2017 Auxetic mechanical metamaterials *RSC Adv.*
- [13] Evans K E and Alderson A 2000 Auxetic materials: Functional materials and structures from lateral thinking! *Adv. Mater.*
- [14] Zheng X, Lee H, Weisgraber T H, Shusteff M, DeOtte J, Duoss E B, Kuntz J D, Biener M M, Ge Q, Jackson J A, Kucheyev S O, Fang N X and Spadaccini C M 2014 Ultralight, ultrastiff mechanical metamaterials *Science (80-.)*.
- [15] Zheng X, Smith W, Jackson J, Moran B, Cui H, Chen D, Ye J, Fang N, Rodriguez N, Weisgraber T and Spadaccini C M 2016 Multiscale metallic metamaterials *Nat. Mater.*
- [16] Meza L R, Das S and Greer J R 2014 Strong, lightweight, and recoverable three-dimensional ceramic nanolattices *Science (80-.)*.
- [17] Torrents A, Schaedler T A, Jacobsen A J, Carter W B and Valdevit L 2012 Characterization of nickel-based microlattice materials with structural hierarchy from the nanometer to the millimeter scale *Acta Mater.*
- [18] Alderson A, Alderson K L, Attard D, Evans K E, Gatt R, Grima J N, Miller W, Ravirala N, Smith C W and Zied K 2010 Elastic constants of 3-, 4- and 6-connected chiral and anti-chiral honeycombs subject to uniaxial in-plane loading *Compos. Sci. Technol.*
- [19] Lorato A, Innocenti P, Scarpa F, Alderson A, Alderson K L, Zied K M, Ravirala N, Miller W, Smith C W and Evans K E 2010 The transverse elastic properties of chiral honeycombs *Compos. Sci. Technol.*
- [20] Chen Y J, Scarpa F, Liu Y J and Leng J S 2013 Elasticity of anti-tetrachiral anisotropic lattices *Int. J. Solids Struct.*

- [21] Lv C, Krishnaraju D, Konjevod G, Yu H and Jiang H 2014 Origami based mechanical metamaterials *Sci. Rep.*
- [22] Al-Mulla T and Buehler M J 2015 Origami: Folding creases through bending *Nat. Mater.*
- [23] Overvelde J T B, Shan S and Bertoldi K 2012 Compaction through buckling in 2D periodic, soft and porous structures: Effect of pore shape *Adv. Mater.*
- [24] Qian W, Yu Z, Wang X, Lai Y and Yellen B B 2016 Elastic metamaterial beam with remotely tunable stiffness *J. Appl. Phys.*
- [25] Valdevit L, Jacobsen A J, Greer J R and Carter W B 2011 Protocols for the optimal design of multi-functional cellular structures: From hypersonics to micro-architected materials *J. Am. Ceram. Soc.*
- [26] Schaedler T A, Ro C J, Sorensen A E, Eckel Z, Yang S S, Carter W B and Jacobsen A J 2014 Designing metallic microlattices for energy absorber applications *Adv. Eng. Mater.*
- [27] Arcaute K, Mann B and Wicker R 2010 Stereolithography of spatially controlled multi-material bioactive poly(ethylene glycol) scaffolds *Acta Biomater.*
- [28] Milton G W and Cherkaev A V. 1995 Which Elasticity Tensors are Realizable? *J. Eng. Mater. Technol.*
- [29] Méjica G F and Lantada A D 2013 Comparative study of potential pentamodal metamaterials inspired by Bravais lattices *Smart Mater. Struct.*
- [30] Moore B, Jaglinski T, Stone D S and Lakes R S 2006 Negative incremental bulk modulus in foams *Philos. Mag. Lett.*
- [31] Grima J N, Attard D, Caruana-Gauci R and Gatt R 2011 Negative linear compressibility of hexagonal honeycombs and related systems *Scr. Mater.*
- [32] Grima J N, Attard D and Gatt R 2008 Truss-type systems exhibiting negative compressibility *Physica Status Solidi (B) Basic Research*
- [33] Cai W, Gładysiak A, Anioła M, Smith V J, Barbour L J and Katrusiak A 2015 Giant Negative Area Compressibility Tunable in a Soft Porous Framework Material *J. Am. Chem. Soc.*
- [34] Mallikarachchi H M Y C and Pellegrino S 2011 Quasi-Static Folding and Deployment of Ultrathin Composite Tape-Spring Hinges *J. Spacecr. Rockets*
- [35] Miller W, Smith C W, MacKenzie D S and Evans K E 2009 Negative thermal expansion: A review *J. Mater. Sci.*
- [36] Munn R W 1972 Role of the elastic constants in negative thermal expansion of axial solids *J. Phys. C Solid State Phys.*
- [37] Wang Q, Jackson J A, Ge Q, Hopkins J B, Spadaccini C M and Fang N X 2016 Lightweight Mechanical Metamaterials with Tunable Negative Thermal Expansion *Phys. Rev. Lett.*
- [38] Qu J, Kadic M, Naber A and Wegener M 2017 Micro-Structured Two-Component 3D Metamaterials with Negative Thermal-Expansion Coefficient from Positive Constituents *Sci. Rep.*
- [39] Ramu S A and Ganesan R 1993 Snapthrough instability of a stochastic a von Mises truss *Arch. Appl. Mech.*
- [40] Antoniadis I, Chronopoulos D, Spitas V and Koulocheris D 2015 Hyper-damping properties of a stiff and stable linear oscillator with a negative stiffness element *J. Sound Vib.*

- [41] Lakes R S, Lee T, Bersie A and Wang Y C 2001 Extreme damping in composite materials with negative-stiffness inclusions *Nature*
- [42] Sarlis A A, Pasala D T R, Constantinou M C, Reinhorn A M, Nagarajaiah S and Taylor D P 2013 Negative Stiffness Device for Seismic Protection of Structures *J. Struct. Eng.*
- [43] Lee C M, Goverdovskiy V N and Temnikov A I 2007 Design of springs with “negative” stiffness to improve vehicle driver vibration isolation *J. Sound Vib.*
- [44] Carneiro V H, Meireles J and Puga H 2013 Auxetic materials - A review *Mater. Sci. Pol.*
- [45] Alderson A and Alderson K L 2007 Auxetic materials *Proc. Inst. Mech. Eng. Part G J. Aerosp. Eng.*
- [46] Saxena K K, Das R and Calius E P 2016 Three Decades of Auxetics Research – Materials with Negative Poisson’s Ratio: A Review *Adv. Eng. Mater.*
- [47] Ebrahimi H, Mousanezhad D, Nayeb-Hashemi H, Norato J and Vaziri A 2018 3D cellular metamaterials with planar anti-chiral topology *Mater. Des.*
- [48] Grima J N and Evans K E 2000 Auxetic behavior from rotating squares *J. Mater. Sci. Lett.*
- [49] Evans K E 2000 Auxetic materials: The positive side of being negative *Eng. Sci. Educ. J.*
- [50] Yang C, Vora H D and Chang Y 2018 Behavior of auxetic structures under compression and impact forces *Smart Mater. Struct.*
- [51] Bezazi A, Boukharouba W and Scarpa F 2009 Mechanical properties of auxetic carbon/epoxy composites: Static and cyclic fatigue behaviour *Phys. Status Solidi Basic Res.*
- [52] Lira C, Innocenti P and Scarpa F 2009 Transverse elastic shear of auxetic multi re-entrant honeycombs *Compos. Struct.*
- [53] Alderson A, Rasburn J, Ameer-Beg S, Mullarkey P G, Perrie W and Evans K E 2000 An auxetic filter: A tuneable filter displaying enhanced size selectivity or defouling properties *Ind. Eng. Chem. Res.*
- [54] Wu W, Song X, Liang J, Xia R, Qian G and Fang D 2018 Mechanical properties of anti-tetrachiral auxetic stents *Compos. Struct.*
- [55] dell’Isola F, Lekszycki T, Pawlikowski M, Grygoruk R and Greco L 2015 Designing a light fabric metamaterial being highly macroscopically tough under directional extension: first experimental evidence *Zeitschrift fur Angew. Math. und Phys.*
- [56] Mohsenizadeh M, Gasbarri F, Munther M, Beheshti A and Davami K 2018 Additively-manufactured lightweight Metamaterials for energy absorption *Mater. Des.*
- [57] Ali M N and Rehman I U 2015 Auxetic polyurethane stents and stent-grafts for the palliative treatment of squamous cell carcinomas of the proximal and mid oesophagus: A novel fabrication route *J. Manuf. Syst.*
- [58] Xue Y, Wang X, Wang W, Zhong X and Han F 2018 Compressive property of Al-based auxetic lattice structures fabricated by 3-D printing combined with investment casting *Mater. Sci. Eng. A*
- [59] Yuan S, Chua C K and Zhou K 2018 3D-Printed Mechanical Metamaterials with High Energy Absorption *Adv. Mater. Technol.*
- [60] Geng L C, Ruan X L, Wu W W, Xia R and Fang D N 2019 Mechanical Properties of Selective Laser Sintering (SLS) Additive Manufactured Chiral Auxetic Cylindrical Stent *Exp. Mech.*

- [61] Jiang Y and Wang Q 2016 Highly-stretchable 3D-architected Mechanical Metamaterials *Sci. Rep.*
- [62] Bückmann T, Stenger N, Kadic M, Kaschke J, Frölich A, Kennerknecht T, Eberl C, Thiel M and Wegener M 2012 Tailored 3D mechanical metamaterials made by dip-in direct-laser-writing optical lithography *Adv. Mater.*
- [63] Farsari M, Vamvakaki M and Chichkov B N 2010 Multiphoton polymerization of hybrid materials *J. Opt.* **12** 124001
- [64] Serbin J, Egbert A, Ostendorf A, Chichkov B N, Houbertz R, Domann G, Schulz J, Cronauer C, Fröhlich L and Popall M 2003 Femtosecond laser-induced two-photon polymerization of inorganic-organic hybrid materials for applications in photonics *Opt. Lett.* **28** 301
- [65] Chichkov B N and Ostendorf A 2006 Two-Photon Polymerization: A New Approach to Micromachining *Photonics Spectra* **40** 72–79
- [66] Lee K S, Yang D Y, Park S H and Kim R H 2006 Recent developments in the use of two-photon polymerization in precise 2D and 3D microfabrications *Polym. Adv. Technol.* **17** 72–82
- [67] Lakes R 1993 Materials with structural hierarchy *Nature*
- [68] Hosford W F and Hosford W F 2012 Tensile Testing *Mechanical Behavior of Materials*
- [69] van Hengel C 2011 Stress-strain curve *Fibre Metal Laminates*
- [70] Hetnarski R B, Ignaczak J and Skrzypek J J 2006 Mathematical theory of elasticity *J. Therm. Stress.*
- [71] Greaves G N, Greer A L, Lakes R S and Rouxel T 2011 Poisson's ratio and modern materials *Nat. Mater.*
- [72] Lee H N, Paeng K, Swallen S F and Ediger M D 2009 Direct measurement of molecular mobility in actively deformed polymer glasses *Science (80-.)*.
- [73] Roundy D and Rogers M 2012 Exploring the thermodynamics of a rubber band *Am. J. Phys.*
- [74] Gutierrez-Lemini D 2014 *Engineering viscoelasticity*
- [75] Weiner J and HO P T 2007 *Light-Matter Interaction* vol 1
- [76] Abbe E 1883 XV.—The Relation of Aperture and Power in the Microscope (continued) *J. R. Microsc. Soc.* **3** 790–812
- [77] Lee K S, Kim R H, Yang D Y and Park S H 2008 Advances in 3D nano/microfabrication using two-photon initiated polymerization *Prog. Polym. Sci.* **33** 631–81
- [78] Farsari M and Chichkov B N 2009 Materials processing: Two-photon fabrication *Nat. Photonics* **3** 450–2
- [79] Tan B, Venkatakrishnan K and Makaronets A 2013 Effects of pulsewidth on two-photon polymerization *Des. Monomers Polym.* **16** 145–50
- [80] Park S H, Yang D Y and Lee K S 2009 Two-photon stereolithography for realizing ultraprecise three-dimensional nano/microdevices *Laser Photonics Rev.* **3** 1–11
- [81] Brinker C J and Scherer G W 1990 *Sol-Gel Science*
- [82] Wu S, Serbin J and Gu M 2006 Two-photon polymerisation for three-dimensional micro-fabrication *J. Photochem. Photobiol. A Chem.* **181** 1–11

- [83] Baldacchini T, LaFratta C N, Farrer R A, Teich M C, Saleh B E A, Naughton M J and Fourkas J T 2004 Acrylic-based resin with favorable properties for three-dimensional two-photon polymerization *J. Appl. Phys.*
- [84] Dimitriadis E K, Horkay F, Maresca J, Kachar B and Chadwick R S 2002 Determination of elastic moduli of thin layers of soft material using the atomic force microscope *Biophys. J.*
- [85] Lemma E D, Rizzi F, Dattoma T, Spagnolo B, Sileo L, Quattieri A, De Vittorio M and Pisanello F 2017 Mechanical Properties Tunability of Three-Dimensional Polymeric Structures in Two-Photon Lithography *IEEE Trans. Nanotechnol.*
- [86] Skarmoutsou A, Lolas G, Charitidis C A, Chatzinikolaidou M, Vamvakaki M and Farsari M 2013 Nanomechanical properties of hybrid coatings for bone tissue engineering *J. Mech. Behav. Biomed. Mater.*
- [87] Meza L R, Zelhofer A J, Clarke N, Mateos A J, Kochmann D M and Greer J R 2015 Resilient 3D hierarchical architected metamaterials. *Proc. Natl. Acad. Sci. U. S. A.*
- [88] Masters I G and Evans K E 1996 Models for the elastic deformation of honeycombs *Compos. Struct.*
- [89] Ma Z-D 2011 Three-dimensional auxetic structures and applications thereof *US Pat. 7,910,193*
- [90] Larsen U D, Sigmund O and Bouwstra S 1997 Design and fabrication of compliant micromechanisms and structures with negative Poisson's ratio *J. Microelectromechanical Syst.*
- [91] Bauer J, Schroer A, Schwaiger R, Tesari I, Lange C, Valdevit L and Kraft O 2015 Push-to-pull tensile testing of ultra-strong nanoscale ceramic-polymer composites made by additive manufacturing *Extrem. Mech. Lett.*